Vol.46 No.1　2022

Journal

JOURNAL OF THE MAGNETICS SOCIETY OF JAPAN

Vol.46 No.1 **2022**
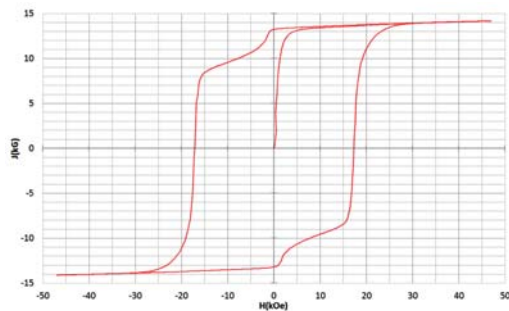
TOEI

世界初！
高温超電導型VSM

新製品

世界初*、高温超電導マグネットをVSMに採用することで
測定速度 当社従来機1/20を実現。
0.5mm cube磁石のBr, HcJ高精度測定が可能と
なりました。
*2014年7月 東英工業調べ

測定結果例

高温超電導VSMによるNdFeB（sint.）0.5mm cube BHカーブ

磁化測定レンジ：0.2emu
Br = 13.2kG   HcJ = 17.2kOe

高温超電導VSMによるNdFeB（sint.）1mm cube BHカーブ
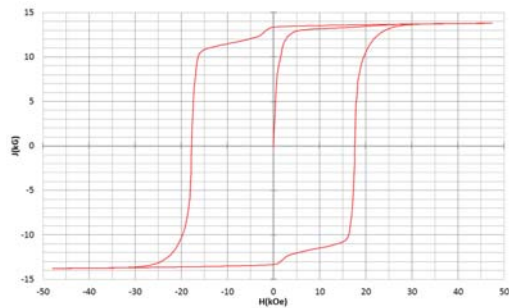
磁化測定レンジ：2emu
Br = 13.3kG   HcJ = 17.7kOe

高温超電導VSMによるNdFeB（sint.）4mm cube BHカーブ
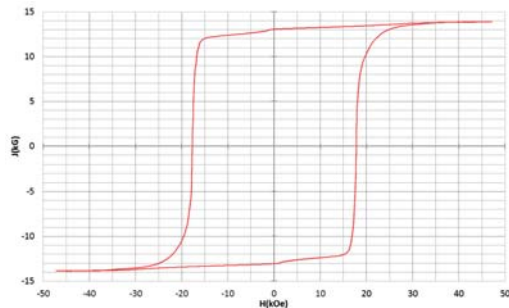
磁化測定レンジ：100emu
Br = 13.1kG   HcJ = 17.8kOe

高速測定を実現

高温超電導マグネット採用により、高速測定を
実現しました。Hmax＝5Tesla, Full Loop測定が
2分で可能です。
（当社従来機：Full Loop測定 40分）

小試料のBr,HcJ高精度測定

0.5mm cube磁石のBr,HcJ高精度測定ができ、
表面改質領域を切り出しBr,HcJの強度分布等、
微小変化量の比較測定が可能です。
また、試料の加工劣化の比較測定が可能です。

試料温度可変測定

－50℃～＋200℃温度可変UNIT（オプション）

磁界発生部の小型化

マグネットシステム部寸法：0.8m×0.3m×0.3m

TOEI 東英工業株式会社

http://www.toeikogyo.co.jp

〒194-0035 東京都町田市忠生1-8-13
TEL：042-791-1211 FAX：042-792-0490
E-mail：sales@toeikogyo.co.jp

Journal of the Magnetics Society of Japan
Vol. 46, No. 1

CONTENTS

<Paper>

Negative Spin-Polarization Tri-Layer STO for MAMR

Ikuya Tagawa

Electrical and Electronic Engineering, Tohoku Institute of Technology, *35-1 Yagiyama-Kasumicho, Sendai 982-8577, Japan*

In microwave-assisted magnetic recording (MAMR), it is still a challenge to obtain a large microwave-assist field (MA field). It is also not easy to enhance the static head field gain (DC gain) brought by the effect of recording flux control. In this paper, we propose a tri-layer spin-torque-oscillator (STO) made of negative spin-polarization material, and we compare the MA field and the DC gain with a conventional dual-layer STO. With this new design, a field generation layer (FGL) can easily obtain stronger spin-transfer torque to overcome the magneto-static interaction with head poles. It works well to increase the DC gain without losing the MA field at lower injection currents. A remaining problem is a significant reduction in the MA field when the injection current becomes too large.

Key words: microwave-assisted magnetic recording, MAMR, spin-torque-oscillator, STO, tri-layer, spin-polarization, negative polarization

1. Introduction

Microwave-assisted magnetic recording (MAMR) is one of the promising technologies for next-generation hard disk drives (HDD) [1-3]. Western Digital and Toshiba have made announcements on their introduction plans of MAMR into production-level HDD [4]. Moreover, Toshiba has announced that they have actually shipped MAMR HDD samples to specific customers [5].

In MAMR, uniform and stable oscillation of the magnetization in a spin-torque-oscillator (STO) is one of the most important factors. We have pointed out that one possible problem in a practical MAMR head is oscillation disturbance by transmitted electron spins from head poles, i.e., a main pole (MP) and a trailing shield (TS). Therefore, we proposed to use negative spin-polarization material in one of head poles [6].

As Toshiba has explained a new concept of MAMR, i.e., FC-MAMR (flux control-microwave-assisted magnetic recording) [7], there is a possibility to obtain static head field gain even without magnetization oscillation in STO. However, if the DC magnetization component of the STO is not oriented to the opposite direction to magnetization of the head poles, this gain can be negative, or loss. In this paper, we show difficulty of avoiding such static field loss in the conventional STO design, and we propose a new design, i.e., a tri-layer STO consisting of three magnetic layers with negative spin-polarization.

2. Modeling

2.1 Head model

A commercial micromagnetics software (Fujitsu Examag v2.1) is used, in which the Landau-Lifshitz-Gilbert (LLG) equation with the spin-transfer torque term is solved [8].

Corresponding author: I. Tagawa (e-mail: i-tagawa@tohtech.ac.jp)
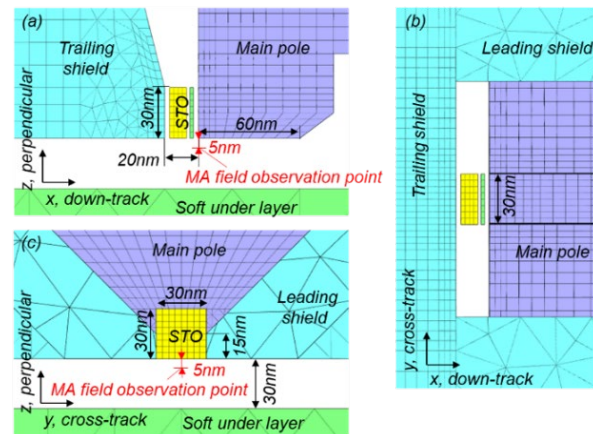
Fig. 1 Pole tip area views of MAMR head model for (a) down-track section, (b) air-bearing surface, (c) cross-track section.

Fig. 1 shows the dimensions of MAMR head model used in analysis. A main pole (MP) and a trailing shield (TS) are divided into hexahedron meshes due to software requirements for calculation of spin-transfer torque between MP and STO, or TS and STO. The STO consists of a spin injection layer (SIL) and a field generation layer (FGL). The SIL is located on the MP side of the FGL. The microwave-assist field (MA field) is evaluated 5 nm below the trailing edge of the MP.

Table 1 Material parameters used in simulation.

	Head MP	Head TS	STO FGL	STO SILs	Media SUL
B_s (T)	2.4	1.6	1.6 (1.0, 2.4)	1.6 (1.0, 2.4)	1.6
H_k (Oe) (*)	10	10	10	10	1000
α, damping	0.05	0.05	0.05	0.05	0.05
A (erg/cm)	3×10^{-6}	2×10^{-6}	2×10^{-6}	2×10^{-6}	2×10^{-6}
P, polarization	0.5	0.5, -0.5	0.5, -0.5	0.5, -0.5	-
t (nm)	-	-	8	2	-

(*) *easy axis: cross track direction*

Other magnetic and geometric properties are summarized in Table 1. Here, α, A, P, and t are the damping constant, magnetic exchange constant, spin polarization factor, and layer thickness, respectively. Even in a tri-layer STO design discussed later, the thickness of two SILs is set at 2 nm and that of the FGL is 8 nm. A rectangular wave current of 100 mA at 1 Gbps frequency is applied to a single-turn head coil.

2.2 Figures of merit

Fig. 2(a) shows a typical example of time-response waveforms of the writing field including the microwave field generated by STO, observed under the main pole edge by 5 nm from the air bearing surface. The down-track field (Hx) shows strong microwave oscillation superposing on the low frequency "quasi-static" field. The cross-track field (Hy) also shows some oscillation, however, there is no clear oscillation in the perpendicular field (Hz), which indicates the microwave field is elliptically rotational in the media plane. Fig. 2(b) shows the Fourier amplitude spectra obtained with FFT. The spectra show clear peaks at about 25 GHz, which are about 1.7 kOe in the down-track field (Hx) and 0.6 kOe in the cross-track field (Hy), respectively. Here, the MA (microwave assist) field amplitude is defined as an averaged value of these two peaks.

As Toshiba has explained in the report [7], the MAMR head has the effect of recording flux control. For quantitative analysis of this effect, the time-averaged writing field profile is calculated as shown in Fig. 2(c), and the quasi-static head field (DC field) magnitude is defined under the main pole inner by 5 nm from the main pole edge. In addition, we have defined the DC field gain which is an increment on the DC field by the flux control effect of STO compared with that of a conventional no-STO head. Note that "conventional head" does not mean "no oscillation of STO" but means "no existence of STO". So, two DC field profiles are calculated and subtraction is made to get the DC field gain.

3. Static Field Gain

3.1 Conventional dual-layer STO

Fig. 3 illustrates design structures near the head pole tip including STO (= FGL + SIL), (a) when STO is connected to TS and MP, and both TS and MP have positive spin-polarizations, (b) when STO is connected to negative polarization TS and positive polarization MP, and (c) when STO is not connected to TS and MP. In the original idea of MAMR [1-2], separate electrodes are connected to STO directly as shown in (c). In contrast, the main pole and the trailing shield are used as electrodes in practical MAMR heads, as shown in (a) and (b), because the write gap is too narrow to fabricate additional electrodes inside. In this situation, electron spins transmitted from the MP to the SIL disturb the
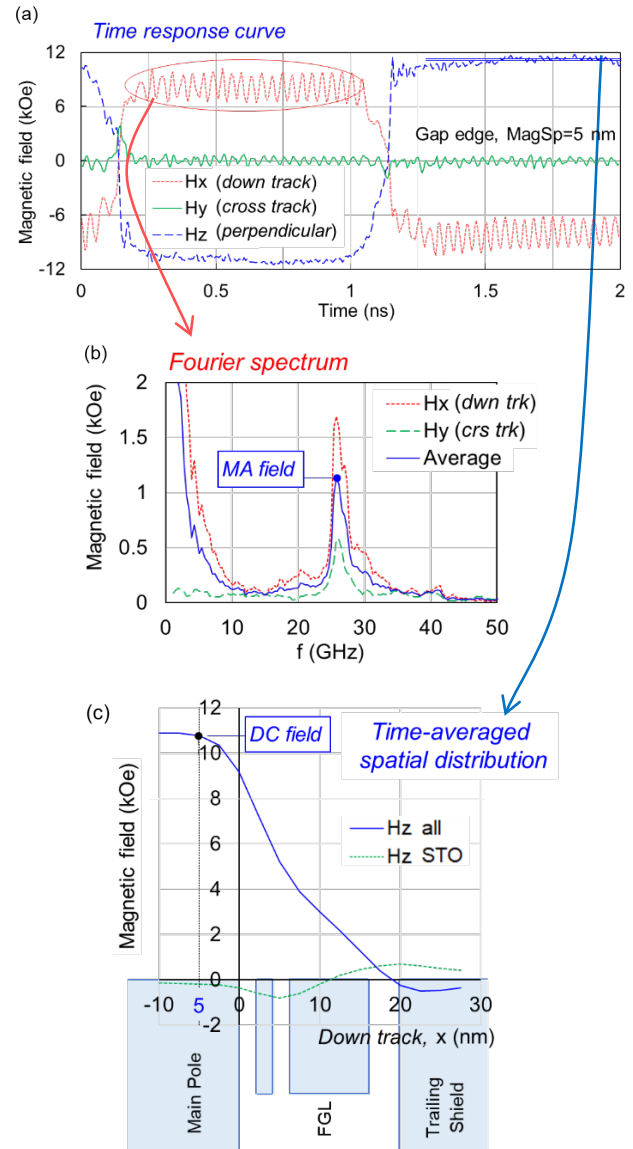
Fig. 2 (a) Time-response waveforms of writing field including STO oscillation field and (b) Fourier amplitude spectra and (c) down track profile of time-averaged perpendicular field.

STO oscillation if they worked to align the SIL magnetization with the MP magnetization.

Fig. 4(a) shows the injection current dependence of the MA field amplitude, for the STO connected to positive polarization TS and MP (▲), for the STO connected to negative polarization TS and positive polarization MP (■), and for the unconnected STO (○), respectively. As we discussed in the previous work [6], no oscillation is observed when electrons flow into the STO from the positive spin-polarization MP (▲). On the other hand, a large MA field is obtained when electrons flow from the negative polarization TS (■). The MA field is even larger than that of the unconnected STO at a lower injection

Fig. 3 Head designs of dual-layer STO connected (a) to positive polarization TS and MP, (b) to negative polarization TS and positive polarization MP, and (c) STO not connected to TS and MP.

current region. This result clearly shows an advantage of the negative polarization TS design.

However, if we look at the DC field gain in Fig. 4(b), we can see that the gain is always negative in the negative polariz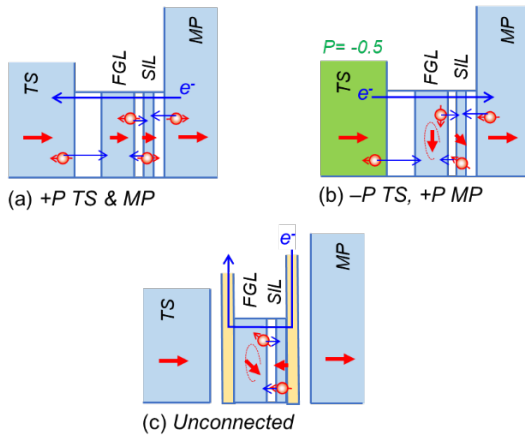ation TS design. Even in the case of the unconnected STO, the DC field gain is very small, and it becomes slightly positive only at very high injection currents.

3.2 Magnetization distribution

Fig. 5 shows magnetization distributions near the head pole tip looked from the media side in the case of (a) the STO connected to negative polarization TS and positive polarization MP and (b) the unconnected STO, respectively, at the injection current of 4×10^8 A/cm^2. The FGL magnetizations tilt towards the cross-track direction but it is not completely in the film plane in both cases of (a) and (b). Therefore, a static component of the down-track FGL magnetization causes the DC field loss, even with good magnetization precession. This indicates that the effect of magneto-static interaction between FGL and TS is still stronger than that of the spin-transfer torque delivered by electrons from TS and SIL. On the other hand, the SIL magnetization is almost opposite to the MP magnetization in the unconnected STO as shown in (b). This means that the magneto-static coupling between SIL and MP could be weak because the SIL thickness is very thin and the total magnetic moment is much smaller than that of the FGL.

4. Tri-layer STO

4.1 Negative polarization tri-layer STO

Based upon the discussion above, another thin SIL between the TS and the FGL looks to be desirable to enjoy larger spin-transfer torque. Actually, a tri-layer
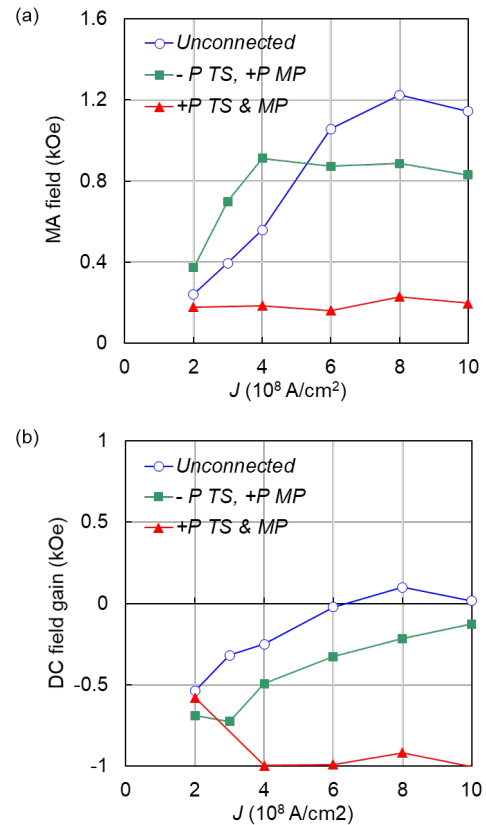
Fig. 4 Injection current dependencies of (a) MA field amplitude and (b) DC field gain in three dual-layer STO designs defined in Fig. 3.
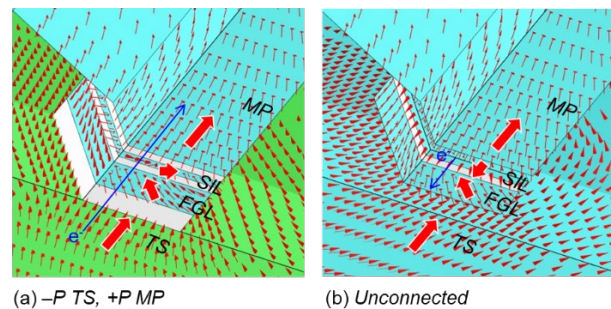
Fig. 5 Magnetization distributions near head pole tip in case of (a) negative polarization TS and positive polarization MP and (b) unconnected STO, respectively.

STO design in which a FGL is sandwiched by two SILs has been proposed by Kanai [9], however, this design didn't work well. The reason is that the spin directions of transmitted electrons from the two adjacent layers are opposite each other as shown in Fig. 6(a). For instance, in the FGL, the spin direction delivered from SIL1 on the left side of MP is opposite to that from SIL2 on the left side of TS. That is why the spin-torque effect is canceled out.

Fig. 6 Head designs of tri-layer STO made of (a) positive and (b) negative polarization materials.

Fig. 7 Injection current dependencies of (a) MA field amplitude and (b) DC field gain, in case of negative and positive polarization tri-layer STOs and dual-layer STO with negative polarization TS.

To avoid this problem, we propose the tri-layer STO made of negative spin-polarization materials as shown in Fig. 6(b). In this design, first, the magnetization direction of the SIL1 is flipped by spin torque of both transmitted electrons through the negative polarization FGL and reflected electrons from the MP. Then, the spin direction of reflected electrons from the SIL1 becomes opposite to the magnetization direction of the MP. The spin direction of transmitted electrons through SIL2 is also opposite to the TS magnetization because of negative polarization. Therefore, it is expected that the FGL can obtain large spin-transfer torque even at lower injection currents.

Negative polarization materials are not well known at present, but there are several academic reports from Tohoku University [10] and Toshiba [11], and Fe_4N, Co_3FeN, and Ni_3FeN materials are referenced in those reports. However, the spin-polarization values of these materials are not clear, so further study is expected.

4.2 Effect in the DC field gain

Fig. 7 shows the injection current dependence of (a) the MA field amplitude and (b) the DC field gain, in the case of the negative polarization tri-layer STO (○)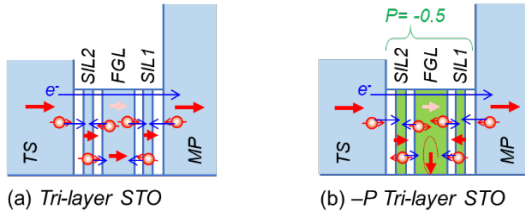, the positive polarization tri-layer STO (▲), and the dual-layer STO with negative polarization TS (■). When all layers have positive polarization in the tri-layer STO (▲), not only no oscillation is observed but also the large DC field loss is shown, even at larger injection currents. On the other hand, in the case of the tri-layer STO with negative polarization (○), the MA field amplitude increases rapidly according to the injection current, though it gets worse when the injection current becomes larger than about 4×10^8 A/cm^2. Moreover, there is a big advantage on the DC field gain. The gain is much larger than that of the dual-layer STO, and it increases up to about 0.5 kOe according to the injection current.

Fig. 8 shows magnetization distributions near the head pole tip looked from the media side in the negative polarization tri-layer STO at the injection current of (a) 4×10^8 A/cm^2 and (b) 6×10^8 A/cm^2, respectively. When the injection current is 4×10^8 A/cm^2, the magnetization in the SIL1 under MP is the opposite of that in the MP. The magnetization in the SIL2 on TS is in the same direction as that in the TS, and the magnetization in the FGL is
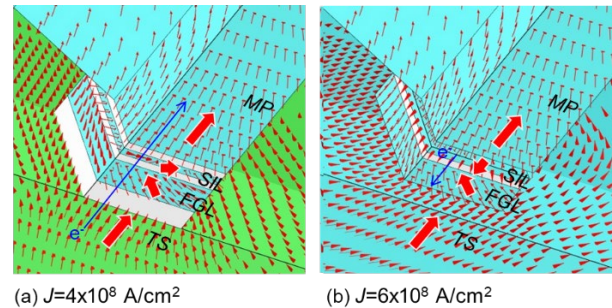
Fig. 8 Magnetization distributions near head pole tip in negative polarization tri-layer STO at injection currents of (a) $J=4\times10^8$, and (b) $J=6\times10^8$ A/cm^2.

in-plane. In this situation, good magnetization precession occurs in the FGL, therefore, the MA field amplitude becomes maximum as shown in Fig. 7(a).

However, when the injection current increases over 4×10^8 A/cm^2, the MA field decreases suddenly. If we looked at the magnetization distribution at 6×10^8 A/cm^2, as shown in (b), we can see that the magnetization in both the SIL1 and the SIL2 are almost in-plane, though anti-

parallel each other. And the FGL magnetization direction is almost opposite to that of the MP. Even the magnetization in the TS is tilted toward the cross-track direction by spin torque of reflected electrons from the SIL2. All these suggest that the spin-transfer torque is too strong for good rotation of the FGL magnetization. Instead, the FGL magnetization easily flips against the magnetizations of the MP and the TS, therefore, we can get the large DC field gain, as shown in Fig. 7(b).

4.3 STO Bs dependence

As discussed above, there is a clear peak on the injection current dependence of the MA field, and at this singular current-point, the DC field gain turns positive from negative. It is supposed that the effect of the spin-transfer torque in the FGL has a good balance with that of the magneto-static interaction between the FGL and the head poles at this singularity. If this is correct, the singular current-point should be changed by the magnetic interaction which is changed by the magnetic moments of the FGL and the SILs.

We have investigated the MA field and the DC field by changing the saturation magnetization (Bs) of STO. Fig. 9 shows injection current dependence of (a) the MA field and (b) the DC field gain when Bs of the FGL and the two SILs are set at 1.0 T, 1.6 T, and 2.4 T, respectively, for the negative polarization tri-layer STO. In the MA field characteristics, the singular current-point giving the peak moves from 2×10^8 A/cm^2 to 6×10^8 A/cm^2 according to the increase of the Bs. And the peak value of the MA field also changes from 0.7 kOe to 1.4 kOe. If we look at the DC field gain characteristics, we can see that the zero cross current-point of the gain also moves from 2×10^8 A/cm^2 to 6×10^8 A/cm^2 consistently with that in the MA field characteristics. From these results, it can be possible to conclude that the lower Bs is preferable to reduce the injection current, but it has a disadvantage of reducing both the MA field amplitude and the DC field gains.

5. Conclusion

We discussed the DC field gain brought by the effect of recording flux control of STO as well as the microwave assist (MA) field generated by the STO oscillation. It was shown that in the conventional dual-layer STO, it is difficult to get the DC field gain even if negative spin-polarization was assumed in the trailing shield (TS), though the reasonably large MA field is obtained. This is because, in the field generation layer (FGL), the effect of the magneto-static interaction with TS is stronger than that of the spin-transfer torque of transmitted electrons. To solve this problem, we proposed the tri-layer STO made of negative polarization material. The new design has worked well to increase the DC field gain without losing the MA field amplitude at lower injection currents. However, a significant decrement of the MA field was shown when the injection current was too large. Further study is needed to achieve the large MF field amplitude and the large DC field gain at the same time.
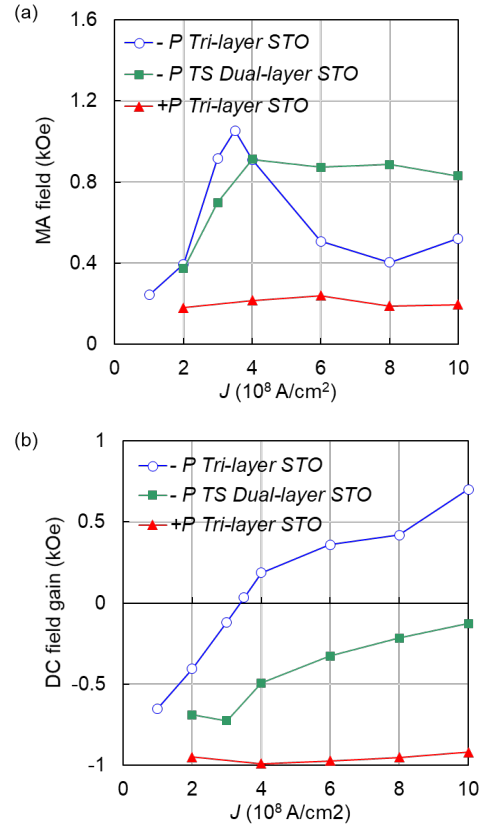

Fig. 9 Injection current dependencies of (a) MA field amplitude and (b) DC field gain, in negative polarization tri-layer STO when Bs was 1.0 T, 1.6 T, and 2.4 T.

References

1). J.-G. Zhu, X. Zhu, and Y. Tang: *IEEE Trans. Magn.*, **44**, 125 (2008)
2). Y. Tang and J. G. Zhu: *IEEE Trans. Magn.*, **44**, 3376 (2008)
3). I. Tagawa, M. Shiimoto, M. Matsubara, S. Nosaki, Y. Urakami and J. Aoyama: *IEEE Trans. Magn.*, **52**, 3101104, (2016)
4). http://innovation.wdc.com/game-changers/why-mamr.html (2017)
5). https://toshiba.semicon-storage.com/jp/company/news/news-topics/2021/02/storage-20210218-1.html (2021)
6). I. Tagawa, *J. Magn. Soc. Jpn.*, **44**, 5 (2020)
7). A. Takeo, *The 31st Magnetic Recording Conference*, C1 (2020)
8). http://www.fujitsu.com/global/about/resources/news/press-releases/2015/0324-01.html (2015)
9). Y. Kanai, R. Itagaki, S. Greaves, H. Muraoka, *MSJ 40th annual conference*, 7pB-4 (2016)
10). M. Tsunoda, Y. Komasaki, S. Kokado, S. Isogami, C. Chen and M. Takahashi.: *Appl. Phys. Express 2*, 083001 (2009)
11). M. Shimizu, K. Koi, S. Murakami, N. Fujita, K. Yamada, and A. Takeo: *MSJ 39th annual conference,* 10pE-3 (2015)

<Paper>

Magnetization Analysis of Magnetic Nanowire Memory
Utilizing Two Recording Metal Wires for Low Current Recording

K. Ogura, M. Takahashi, N. Nakatani, N. Ishii, and Y. Miyamoto

Science & Technology Research Laboratories, *NHK* (Japan Broadcasting Corporation)

1-10-11 Kinuta, Setagaya-ku, Tokyo 157-8510, Japan

We have developed magnetic nanowire memories with no mechanical moving parts in order to achieve the large-capacity and ultra-high data transfer rates required for spatial imaging three-dimensional television (3D-TV). In a magnetic nanowire, binary information is recorded by means of a magnetic field induced by two recording wires that are orthogonally fabricated above the nanowire. We simulated the magnetic domain formation process and found that it was formed stably in a magnetic nanowire when we utilized two recording wires. In addition, by adding a certain time difference to the current, the magnetic domains were formed with low current density. We analyzed the behavior inside the magnetic nanowire and found that magnetization reversal can be achieved at low current density when torque is applied at the appropriate time during the precession of the magnetic moment.

Key words: magnetic nanowire memory, magnetization reversal, magnetic domains, current-driven domain wall motion

1. Introduction

We have been developing magnetic storage devices that work with huge amounts of data at ultra-high speed to be utilized for future 3D-TV storage. Since the data transfer rate required for storage devices in spatial imaging 3D-TVs [1] (light field spatial imaging) is expected to exceed at 1 Tbps, which is far faster than that of uncompressed ultra-high definition TV (144 Gbps), it is extremely difficult to utilize existing memories, such as HDDs or SSDs. There is therefore a need to develop a new one that has both a large capacity and a high transfer rate, and that can hold data for a long time. Many researches on utilizing a magnetic nanowire as a memory have been reported [2]–[4] in recent years and they are also promising candidates for future 3D-TV storage devices. Unlike HDDs, which have a magnetic head and a disk drive mechanism, magnetic nanowire memories contain no mechanically moving parts and domain walls are driven at high speed by spin transfer torque [5]. Also, by synchronizing the parallel operation of many nanowires, they have the advantage of further high data transfer rate [6]–[8].

We have already succeeded in driving multiple magnetic domains along magnetic nanowire [9-12] and forming magnetic domains in nanowire by magnetic recording head used in HDD [13]. However, in order to use it as a real device, it is necessary to form magnetic domains at a lower recording current and all the components, *i.e.* magnetic nanowire media, insulator, writer and readers, should be integrated onto silicon wafer substrates. For the racetrack memory, writing data is accomplished by a current magnetic field induced by a single metal wire [14]. We consequently developed a recording method utilizing two metal wires for stable and low current domain formation [15]. In this study, we propose a method for adding a time difference to the current applied to the two metal wires and managed to record binary information at a lower current. The purpose of this work is to analyze the behavior of the magnetic moment and to determine the mechanism underlying the lower current recording.

2. Magnetic nanowire memory

As shown in Fig. 1, the memory consists of a large number of magnetic nanowires, which are fabricated to be a couple of hundred nanometers wide and two recording metal wires. The recording wires are orthogonally arranged above the magnetic nanowires. The flow of the memory operation is as follows: First, we apply a magnetic field induced from each recording wire to the magnetic nanowires by sending a pulse current to each recording wire in the opposite direction. Magnetic domains are then formed directly below the gap between the two recording wires using the synthesized magnetic field to record information. Next, a driving pulse current is applied to the left side of the magnetic nanowire to shift the magnetic domains at high speed. By repeating these recording and driving operation, the magnetic nanowire accumulates the magnetic domains. Finally, these stored magnetic domains are detected and reproduced with a tunnel magnetoresistance (TMR) head.
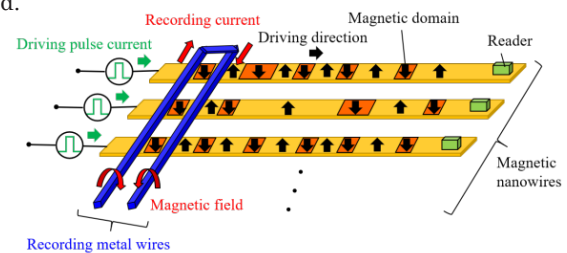

Fig. 1 Magnetic nanowire memory.

Corresponding author: K. Ogura mail:ogura.k-ja@nhk.or.jp

3. Micromagnetic simulation

3.1 Simulation model

We analyzed the behavior of the magnetic moment during the magnetic domain formation process by micromagnetic simulation using the Landau-Lifshitz-Gilbert (LLG) equation. The nanowire model used in the calculation is shown in Fig. 2. The magnetic nanowire is rectangular and measures 1.6 µm long, 120 nm wide (W_m), and 12 nm thick (H_m). The recording wire is 2 µm in length (L_r) and has a 120-nm square on each side in cross section (W_r, H_r). The gap between the two recording wires is 100 nm (S_p), and an air gap between the recording wires and the magnetic nanowires as an insulating layer is 10 nm. The magnetic nanowire was divided into 4nm cube meshes for calculation from the perspective of calculation accuracy.

3.2 Simulation conditions

The recording currents I_A and I_B (current density: j) shown in Fig. 3 were respectively applied to recording wires A and B in the opposite direction with a time difference T. We calculated the magnetic domain formation below the gap after 2 ns of applying the current. The parameters of the recording current and the magnetic properties of the magnetic nanowire are listed in Table 1. The initial magnetization direction was set to the +z direction.
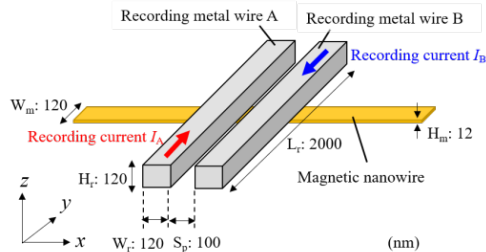

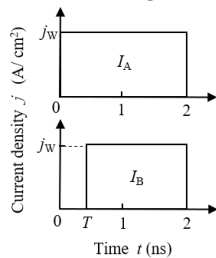**Fig. 2** Simulation model of magnetic nanowire memory.

Fig. 3 Pulse diagrams of recording current applied to two metal recording wires. The current density of I_A and I_B is set so that magnetization reversal cannot occur when I_A and I_B are applied simultaneously without time difference.

3.3 Simulation results

Fig. 4 shows the analysis results of the magnetization after 2 ns of the current applied to two recording wires. For (a) a single recording wire, the left end of the magnetic wall was stable and formed a straight line. However, the right edge of the domain wall was swaying throughout the calculation and was not stable at the

Table 1 Magnetic properties and recording current parameters of magnetic nanowire.

Magnetic nanowire		Recording current	
Anisotropic magnetic field: H_k (kOe)	5	Pulse width: (ns)	I_A: 2
			I_B: 2-T
Exchange coupling constant: A (J/m)	1.2×10^{-11}	Current density: j_w (A/cm^2)	3.3×10^8
Saturation magnetization: $4\pi M_s$ (T)	0.15		

end, indicating that more time was required for the magnetic domain to stabilize. In this case, the recording currents of 110 mA which is the minimum value to successfully form the magnetic domain was applied. In contrast, for (b), when recording currents I_A and I_B were applied to the recording wires in the opposite direction with no time difference, the minimum recording current was around 60 mA which is lower than the current needed for a single recording wire. Moreover, when recording currents were applied with a time difference of $T = 0.15$ ns the minimum recording current was around 50 mA, which means we succeeded in reducing the recording current by 10 mA. This was because the magnetic field induced by the current was generated symmetrically from each recording wire, and the z component of the synthetic magnetic field was uniformly distributed around the gap between the two recording wires.

Next, to examine the tolerance, we calculated the magnetic domain formation in the case when the pulse currents I_A and I_B, shown in Fig. 3, were applied to the recording wires A and B in the opposite directions with a time difference of $T = 0$–0.25 ns (0.01 ns step). We found that the magnetic domain was specifically formed at around $T = 0.05$ ns and $T = 0.15$ ns. Fig. 5 shows the magnetic domain formation after 2 ns of the current applied to the recording wires. These results demonstrate that it is possible to reverse the magnetization in the magnetic nanowires just below the recording gap in the range of time differences $T = 0.03$–0.08 ns and $T = 0.15$–0.18 ns, and that there was a difference in each magnetic domain formation process. In this paper, we focus on the typical behavior of the magnetic moment at $T = 0.15$ ns, as the clearest simulation results of magnetization reversals including nucleation and domain wall propagation were obtained for this timing.
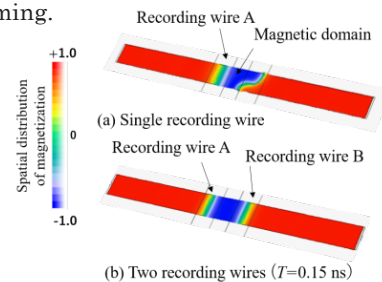

Fig. 4 Spatial distributions of magnetizations at elapsed time of 2 ns.

4. Analysis of magnetization reversals

Fig. 6 shows the spatial distribution of the magnetizations after 0.1 ns in the process of magnetic domain formation when the time difference of $T = 0.15$ ns was provided. We can see that the magnetization reversal at the α point (50 nm, –58 nm, 6 nm), which is the core of the magnetic domain formation, was induced at first, and then a reversed magnetic domain was spread and formed in the entire gap between the recording wires by diffusion propagation of the magnetic wall [16]. We therefore focused our analysis on the temporal changes of the magnetic moment at α point and at β point (2 nm, 2 nm, 6 nm), which is near the origin, as the representative points of the propagation.
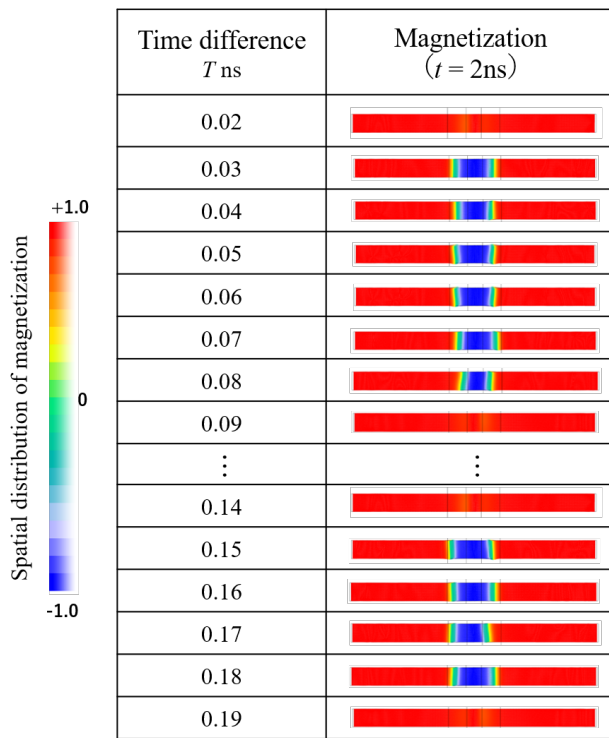
Time difference T ns	Magnetization ($t = 2$ns)
0.02	
0.03	
0.04	
0.05	
0.06	
0.07	
0.08	
0.09	
⋮	⋮
0.14	
0.15	
0.16	
0.17	
0.18	
0.19	

Spatial distribution of magnetization: +1.0, 0, -1.0

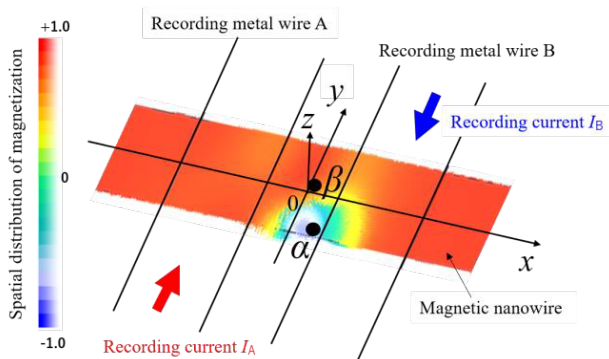**Fig. 5** Spatial distributions of magnetization at each time difference.

Fig. 6 Nucleation and magnetic wall propagation by recording current with the time difference $T = 0.15$ ns.

The magnetization trajectory at the time of magnetization reversal at α and β points is shown in Fig. 7. At α point (red line), precession was induced in the magnetic moment after the current was applied to recording nanowires, and the magnetic moment reversed after passing through a complicated path several times while pointing in the +z direction. Since α point was the core of the magnetization reversal (as described above), whether or not magnetic domains were formed in the gap depended on the feasibility of the magnetization reversal at α point. On the other hand, at β point (blue line), the magnetic wall propagated due to the interaction of the magnetic moments between the neighboring meshes and the magnetic reversals occurred in a short time.

Fig. 8 shows the time variation of the z-component of the magnetic moment after the recording current I_A was applied. Here, the magnetization trajectory that occurred when recording current I_A was applied at $t = 0$ and I_B was applied with a time difference of $T = 0.14$–0.19 ns is also shown. For the time differences of $T = 0.14$ ns and $T = 0.19$ ns (dotted lines), the magnetic moment failed to reverse even after the torque was applied by the recording current I_B. In contrast, in the range of $T = 0.15$–0.18 ns (solid line), the magnetic moment succeeded in reversing, which indicates that the magnetization reversed while oscillating in the z direction. When we examined the first time at which the z-component of the magnetic moment turned negative, *i.e.*, below zero, we found that magnetization reversal in the case of $T = 0.16$ ns and 0.17 ns commenced in a relatively short time ($t = 0.25$ ns).

In the range of $T = 0.15$–0.18 ns, where magnetization reversal occurred, there was a slight difference in the process of reversal depending on the time difference T. This indicates that the feasibility of the magnetization reversal is related to the position at which the recording current I_B applied the torque to the precession of the magnetic moment at α point. Therefore, we next investigated the relationship between the magnetization trajectory and the time when the torque superposition commenced.

The magnetization trajectory at α point, the core of the magnetic domain formation, is shown on the x-y plane in Fig. 9. First, the magnetic moment started its precession from the origin, and after drawing a larger circle counterclockwise for 0.11 ns, it entered the second track. Here, we overlay the magnetization trajectory when the recording current I_B was applied with the time difference $T = 0.14$–0.19 ns. We found that when a torque was applied to the precession of the magnetic moment, the subsequent magnetization trajectory changed in accordance with the time difference T. At the time difference T indicated by the red dotted line, magnetization reversed in a relatively wider range on the left side of the larger magnetization trajectory (second and third quadrants) and in a narrow range on the left side of the second track of the precession.

Our future work will involve investigating the physical significance of the optimal torque position (in the range of 150–225°) for the precession.
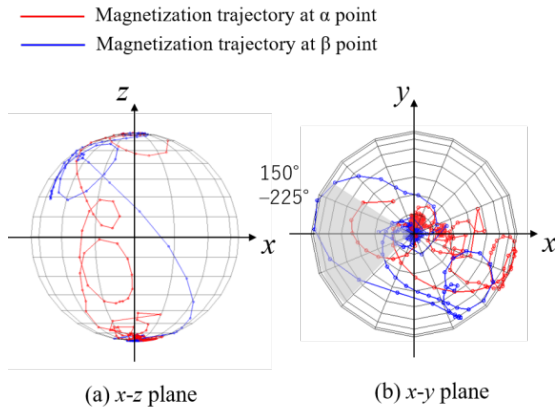

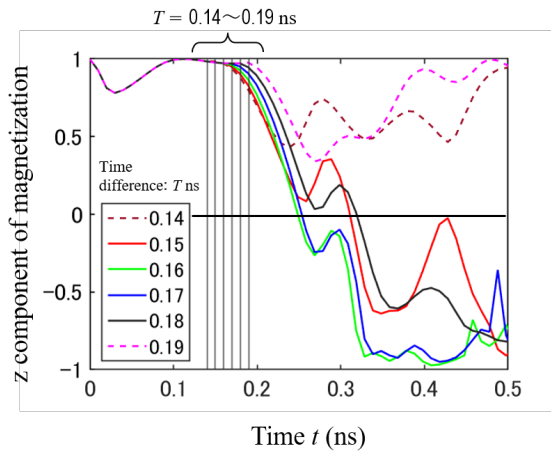**Fig. 7** Magnetization trajectory at analysis points.

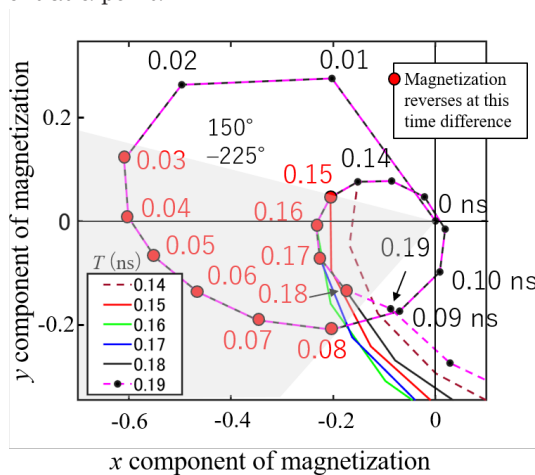**Fig. 8** Time variation of z component of magnetic moment at α point.

Fig. 9 In-plane magnetization trajectory at α point.

4. Conclusion

We have proposed a magnetic nanowire memory with two recording wires and analyzed the magnetic domain formation process by micromagnetic simulation. Results showed that magnetic domains were successfully formed by low current density in a magnetic nanowire when a current in the opposite direction with an appropriate time difference was applied to the recording wires. We analyzed the behavior of the magnetization to determine the appropriate range of the time difference and found that there was a close relationship between the precession and the position where the torque was applied by the current I_B, and that the magnetization reversed in a specific range on the magnetization trajectory.

Overall, we demonstrated that our method of forming magnetic domains by controlling the time difference between the currents applied to the two recording wires is very useful. In a real device, it is possible to adjust the time difference between the two recording currents with an ultrashort pulse generator, or to determine the extra length of the U-shaped recording wire to create the appropriate time difference.

In future work, we will conduct a more detailed analysis and verify the range of the time difference in the case of multiple interacting magnetic nanowires.

References

1) R. Higashida, N. Funabashi, K. Aoshima, and K. Machida: *IEEE Trans. Magn.*, **4**, 1 (2021).
2) Kab-Jin Kim, D. Chiba, K. Kobayashi, S. Fukami, M. Yamanouchi, H. Ohno, Soong-Geun Je, Sug-Bong Choe, and T. Ono: *Appl. Phys. Lett.* **101**, 022407 (2012).
3) H. Tanigawa, T. Koyama, G. Yamada, D. Chiba, S. Kasai, S. Fukami, T. Suzuki, N. Ohshima, N. Ishiwata, Y. Nakatani: *Appl. Phys. Express*, **2**, 053002 (2009).
4) Y. M. Hung, T. Li, R. Hisatomi, Y. Shiota, T. Moriyama, T. Ono: *J. Magn. Soc. Jpn.* **45**, 6 (2021).
5) A. Yamaguchi, T. Ono, S. Nasu, K. Miyake, K. Mibu, and T. Shinjo: *Phys. Rev. Lett.*, **92**, 077205 (2004).
6) M. Hayashi, L. Thomas, C. Rettner, R. Moriya, Y. B. Bazally, and S. S. P. Parkin: *Phys. Rev. Lett.*, **98**, 037204 (2007).
7) I. M. Miron, T. Moore, H. Szambolics, L. D. Buda-Prejbeanu, S. Auffret, B. Rodmacq, S. Pizzini, J. Vogel, M. Bonfim, A. Schuhl, and G. Gaudin: *Nat. Mater.*, **10**, 419 (2011).
8) S. Yang, K. Ryu, and S. Parkin: *Nat. Nanotechnol.*, **10**, 221 (2015).
9) M. Okuda, Y. Miyamoto, M. Kishida, and N. Hayashi: *IEEE Trans. Magn.*, **47**, 2525 (2011).
10) M. Okuda, Y. Miyamoto, E. Miyashita, and N. Hayashi: *J. Appl. Phys.*, **115**, 17D113 (2014).
11) M. Okuda, Y. Miyamoto, E. Miyashita, and N. Hayashi: *J. Jpn. Soc. Powder Powder Metall.*, **61**, S37 (2014).
12) M. Okuda, Y. Miyamoto, E. Miyashita, N. Saito, N. Hayashi, and S. Nakagawa: *J. Appl. Phys.*, **117**, 17D516 (2015).
13) M. Okuda, Y. Miyamoto, M. Kawana, E. Miyashita, N. Saito, and S. Nakagawa: *IEEE Trans. Magn.*, **52**, 3401204 (2016).
14) S. S. P. Parkin, M. Hayashi, and L. Thomas: *Science*, **320**, 190 (2008).
15) M. Kawana, M. Okuda, Y. Miyamoto: Kokai Tokkyo Koho JP 2020-027805 (2020).
16) V. Zhukova, J. M. Blanco, V. Rodionova, M. Ipatov, and A. Zhukov: *J. Appl. Phys.* **111**, 07E311 (2012).

<Paper>

Information Degradation during Archiving in Heat-Assisted Magnetic Recording

T. Kobayashi, Y. Nakatani*, and Y. Fujiwara

Graduate School of Engineering, Mie Univ., *1577 Kurimamachiya-cho, Tsu 514-8507, Japan*

*Graduate School of Informatics and Engineering, Univ. of Electro-Communications, *1-5-1 Chofugaoka, Chofu 182-8585, Japan*

We examine the dependence of information stability on certain medium parameters, namely mean Curie temperature, grain height, and anisotropy constant ratio in 4 Tbpsi heat-assisted magnetic recording, for 10 years of archiving. We introduce a minimum normalized readout field H_0 after 10 years of archiving and an information degradation rate R_0 during 10 years of archiving. To interpret the results, we investigate whether there is a correlation between H_0 or R_0 and an effective thermal stability factor for 9 and 6 grains/bit. We find that there is a strong correlation since the anisotropy constant is much larger than the shape anisotropy. The H_0 and R_0 values are functions of the effective thermal stability factor and grain number, and are independent of grain number per bit. The effective thermal stability factor necessary for no information degradation is more than about 120. Furthermore, there is a weak correlation between the initial readout field or minimum readout field after 10 years of archiving and the effective thermal stability factor.

Key words: HAMR, bit error rate, degradation rate, thermal stability factor, grain number

1. Introduction

The long-term stability of archived information is one of the most important properties of magnetic recording media. This stability has been widely discussed using the thermal stability factor $K_u V/(kT)$, where K_u, V, k, and T are the grain anisotropy constant, grain volume, Boltzmann constant, and temperature, respectively[1]. Heat-assisted magnetic recording (HAMR) is a promising candidate as a next generation magnetic recording method that can operate beyond the trilemma limit[1]. HAMR is a recording method in which the medium is heated to reduce coercivity during the writing period. We have introduced an HAMR medium parameter, namely, the medium anisotropy constant ratio K_u/K_{bulk} [2] in place of the medium anisotropy constant K_u since the K_u value at the storage temperature is a function of the medium Curie temperature T_c, which is strongly related to the writing property. K_u/K_{bulk} is the intrinsic ratio of the medium K_u to bulk FePt K_u regardless of T_c where FePt is a candidate HAMR medium material thanks to its large K_u and relatively low T_c.

We have already calculated the numerical values of $K_u V/(kT)$ and K_u/K_{bulk} necessary for 10 years of archiving in 2 Tbpsi HAMR by employing a bit error rate calculation using the grain error probability[3]. We used an error (signal) threshold of 0.5 as a calculation condition.

In this paper, we estimate the minimum normalized readout field related to the minimum error threshold, that must be readable without error after 10 years of archiving in 4 Tbpsi HAMR. Furthermore, we also

examine the information degradation rate during 10 years of archiving. The mean Curie temperature T_{cm} affects various properties in HAMR. The larger grain aspect ratio h/D_m of the grain height (medium layer thickness) h to the mean grain size D_m appears to make it too difficult to manufacture the medium. Furthermore, there is a concern that K_u, namely, K_u/K_{bulk} decreases as D_m decreases. Thus, we examine the dependence of information stability on the medium parameters T_{cm}, h, and K_u/K_{bulk}.

2. Calculation Method and Conditions

2.1 Magnetic properties

The temperature dependence of the magnetization M_s was calculated by employing a mean field analysis[4], and that of the anisotropy constant K_u was assumed to be proportional to M_s^2 [5]. $M_s(T_c, T)$ is a function of T_c and T. And $M_s(T_c = 770\,\text{K}, T = 300\,\text{K}) = 1000\,\text{emu/cm}^3$ was assumed for FePt. With this assumption, the M_s value can be calculated for all T_c and T values.

The anisotropy constant $K_u(T_c, K_u/K_{bulk}, T)$ is a function of T_c, K_u/K_{bulk}, and T. And $K_u(T_c = 770\,\text{K}, K_u/K_{bulk} = 1, T = 300\,\text{K}) = 70\,\text{Merg/cm}^3$ was assumed for bulk FePt. With this assumption, the K_u value can be calculated for all T_c, K_u/K_{bulk}, and T values. No intrinsic distribution of K_u was assumed. However, there was a fluctuation in K_u caused by T_c variation.

The T_c value can be adjusted by changing the Cu composition z for $(\text{Fe}_{0.5}\text{Pt}_{0.5})_{1-z}\text{Cu}_z$.

2.2 Field strength

The recording density is 4 Tbpsi, and the bit area S is 161 nm^2. We assumed the medium to be granular. One bit has m grains in the cross-track direction and n grains in the down-track direction, namely, there are $m \times n$ grains/bit. The mean grain size D_m was

determined by

$$D_{\mathrm{m}} = \sqrt{\frac{S}{m \times n}} - \Delta_{\mathrm{G}}, \qquad (1)$$

where Δ_{G} is the intergrain spacing. The bit aspect ratio is $D_{\mathrm{T}}/D_{\mathrm{B}} = m/n$ where $D_{\mathrm{T}} = m(D_{\mathrm{m}} + \Delta_{\mathrm{G}})$ and $D_{\mathrm{B}} = n(D_{\mathrm{m}} + \Delta_{\mathrm{G}})$ are the track width and bit pitch, respectively. The flying height $h_{\mathrm{fly}} = 4.0$ nm is the distance between the magnetic head reader and the recording layer surface.

The magnetic field strength from the medium at the center of m grains and the reader position was calculated using $m \times 30$ grains with no grain size distribution when calculating the field strength.

2.3 Bit error rate

The bit error rate bER was calculated by employing each grain error probability P_i,

$$P_i = 1 - \exp\left(-f_0 t \exp\left(-\frac{K_{\mathrm{ueff}}V}{kT}\right)\right), \qquad (2)$$

taking account of the shape anisotropy $M_s H_{\mathrm{d}}/2$ using a self-demagnetizing field H_{d} where f_0, $t = 10$ years, and K_{ueff} are the attempt frequency[6], time, and effective anisotropy constant, respectively. And $K_{\mathrm{ueff}} = K_{\mathrm{u}} - M_s H_{\mathrm{d}}/2$, $H_{\mathrm{d}} = 8M_s \arctan\left(D^2/(h\sqrt{2D^2 + h^2})\right)$, $V = D \times D \times h$ where D is the grain size. Since H_{d} does not affect the results as mentioned below, the magnetostatic field from surrounding grains can also be ignored. It was assumed that there is no exchange coupling between grains. For example, for 4 grains/bit, the 1 grain-error bit error rate $_4\mathrm{bER}_1$ is expressed as

$$\begin{aligned}_4\mathrm{bER}_1 = \ &Er_1 P_1(1 - P_2)(1 - P_3)(1 - P_4) + \cdots \\ &+ Er_4(1 - P_1)(1 - P_2)(1 - P_3)P_4, \end{aligned} \qquad (3)$$

the 2 grain-error bit error rate $_4\mathrm{bER}_2$ as

$$\begin{aligned}_4\mathrm{bER}_2 = \ &Er_{12} P_1 P_2(1 - P_3)(1 - P_4) + \cdots \\ &+ Er_{34}(1 - P_1)(1 - P_2)P_3 P_4, \end{aligned} \qquad (4)$$

the 3 grain-error bit error rate $_4\mathrm{bER}_3$ as

$$\begin{aligned}_4\mathrm{bER}_3 = \ &Er_{123} P_1 P_2 P_3(1 - P_4) + \cdots \\ &+ Er_{234}(1 - P_1)P_2 P_3 P_4, \end{aligned} \qquad (5)$$

and the 4 grain-error bit error rate $_4\mathrm{bER}_4$ as

$$_4\mathrm{bER}_4 = P_1 P_2 P_3 P_4, \qquad (6)$$

where

$$Er_k = 1, \text{ if } \frac{\sum_{i,j} M_{sij}(T_{cij}, \ 330 \text{ K})D_{ij}^2}{(m \times n)M_{\mathrm{s}}(T_{\mathrm{cm}}, \ 330 \text{ K})D_{\mathrm{m}}^2} \le E_{\mathrm{th}}, \quad (7)$$

and

$$Er_k = 0, \text{ if } \frac{\sum_{i,j} M_{sij}(T_{cij}, \ 330 \text{ K})D_{ij}^2}{(m \times n)M_{\mathrm{s}}(T_{\mathrm{cm}}, \ 330 \text{ K})D_{\mathrm{m}}^2} > E_{\mathrm{th}}. \quad (8)$$

Errors occur in some grains of a bit. We assumed that if the ratio of $\sum_{i,j} M_{sij}(T_{cij}, \ 330 \text{ K})D_{ij}^2$ to $(m \times n)M_{\mathrm{s}}(T_{\mathrm{cm}}, \ 330 \text{ K})D_{\mathrm{m}}^2$ in Eqs. (7) and (8) is more than the error threshold E_{th}, the bit is error-free after 10 years of archiving where the numerator $\sum_{i,j} M_{sij}(T_{cij}, \ 330 \text{ K})D_{ij}^2$ is the surface magnetic charge of the grains for which the magnetization turns in the recording direction, and the denominator $(m \times n)M_{\mathrm{s}}(T_{\mathrm{cm}}, \ 330 \text{ K})D_{\mathrm{m}}^2$ is the total surface magnetic charge at the readout temperature of 330 K. M_{sij}, T_{cij}, and D_{ij} are the magnetization, the Curie temperature, and the grain size of the ij-th grain, respectively. The total bit error rate $_4\mathrm{bER}$ is the summation of each bit error rate $_4\mathrm{bER}_k$ as follows

$$_4\mathrm{bER} = \Sigma_k {}_4\mathrm{bER}_k. \qquad (9)$$

The calculation bit number was 1E+7. The criterion determining whether or not information is stable was assumed to be a bER of 1E−3.

The minimum normalized readout field H_0 after 10 years of archiving can roughly be represented by E_{th} as

$$H_0 = 2E_{\mathrm{th}} - 1. \qquad (10)$$

We defined the information degradation rate R_0 during 10 years of archiving as

$$R_0 = \frac{\mathrm{bER(10.0 \ yrs)} - \mathrm{bER(0.001 \ yrs)}}{\mathrm{bER(0.001 \ yrs)}}. \qquad (11)$$

For example, the R_0 values are 99, 9.0, and 0.25 when the bER(0.001 yrs) values are 1E−5, 1E−4, and 8E−4, respectively, since the bER(10.0 yrs) value is 1E−3. The R_0 value for no information degradation is less than about 0.25.

The conditions used when calculating the bER are summarized in Table 1. We assumed that the intergrain spacing Δ_{G} was 1.0 nm. The grain size distribution was log-normal with a standard deviation $\sigma_{\mathrm{D}}/D_{\mathrm{m}}$ of 15 %, and the T_{c} distribution was normal with a standard deviation $\sigma_{\mathrm{Tc}}/T_{\mathrm{cm}}$ of 2 %. The attempt frequency f_0 is a function of the Gilbert damping constant α[6], and we used an α value of 0.1. The storage temperature T_{sto} was 350 K since we take a certain margin for temperature into account.

Table 1 Conditions for bit error rate calculation.

Recording density (Tbpsi)	4
Intergrain spacing Δ_{G} (nm)	1.0
Standard deviation $\sigma_{\mathrm{D}}/D_{\mathrm{m}}$ (%) of D_{m}	15
Standard deviation $\sigma_{\mathrm{Tc}}/T_{\mathrm{cm}}$ (%) of T_{cm}	2
Gilbert damping constant α	0.1
Storage temperature T_{sto} (K)	350

3. Calculation Results

3.1 Various medium parameters

The bER value as a function E_{th} and H_0 after 10 years of archiving for various T_{cm} values in $m \times n = 3 \times 3 = 9$ grains/bit is shown in Fig. 1 (a) where $h = 10.5$ nm and $K_{\mathrm{u}}/K_{\mathrm{bulk}} = 0.8$. The bER value increases as the

T_{cm} value decreases. There is no E_{th} more than 0.5, namely, no H_0 more than 0 that satisfies bER = 1E−3 for T_{cm} = 600 K. The time dependence of the bER is shown in Fig. 1 (b) where 0.001 years corresponds to about 9 hours. Errors increase over time for T_{cm} = 650 K, therefore the initial bER before archiving must be low, for example, 1E−4. On the other hand, the error scarcely increases for T_{cm} = 750 K.
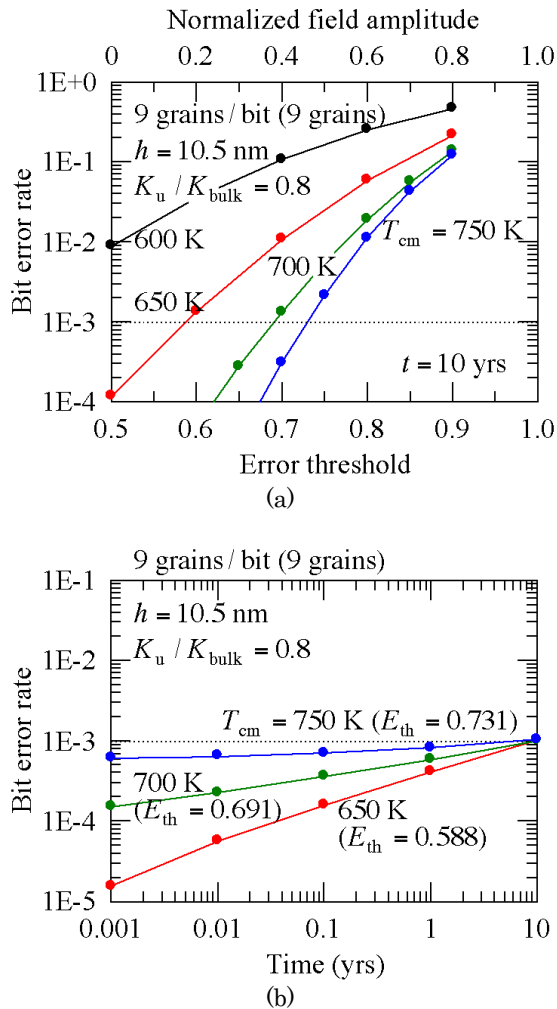

Fig. 1 (a) Bit error rate as a function of error threshold and normalized field amplitude after 10 years of archiving and (b) time dependence of bit error rate during 10 years of archiving for various mean Curie temperatures T_{cm} (h = 10.5 nm and K_u/K_{bulk} = 0.8).

Figure 2 shows (a) the z component H_z of the initial readout field for the down-track direction and (b) the minimum readout field $H_0 \times H_z$ that must be readable without error after 10 years of archiving. Although the error scarcely increases for T_{cm} = 750 K as shown in Fig. 1 (b), the $H_0 \times H_z$ value is small as shown in Fig. 2 (b). This means that the error is caused by the cluster of small grains. The grain number per bit may increase at that time, and the $H_0 \times H_z$ value may be larger. This problem is a future subject for study. In contrast, since errors increase over time for T_{cm} = 650 K as shown in

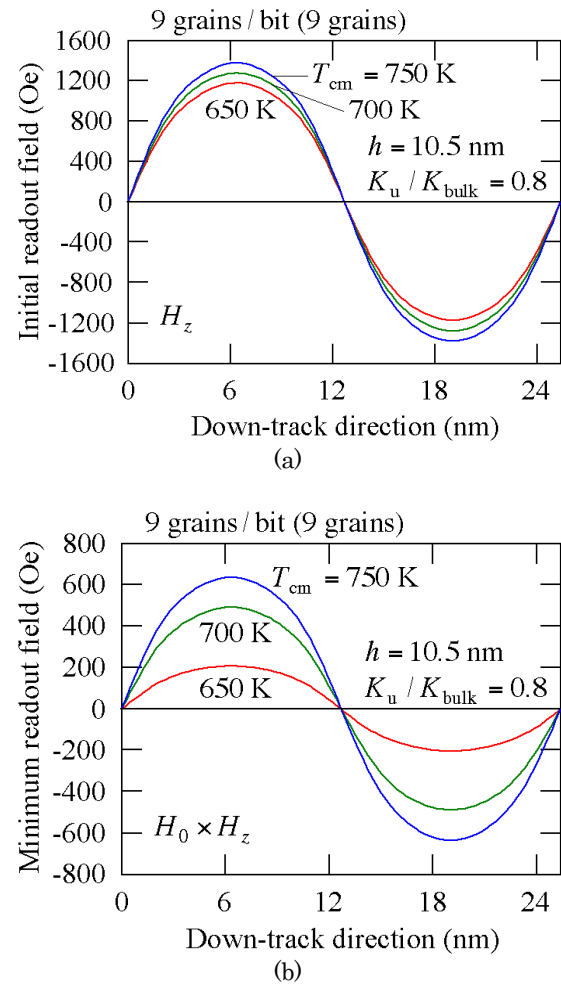Fig. 1 (b), the $H_0 \times H_z$ value becomes small as shown in Fig. 2 (b).

Fig. 2 (a) Initial readout field H_z and (b) minimum readout field $H_0 \times H_z$ after 10 years of archiving for various mean Curie temperatures T_{cm} (h = 10.5 nm and K_u/K_{bulk} = 0.8).

If T_{cm} = 750 K, h = 6.5 nm, and K_u/K_{bulk} = 0.8, or if T_{cm} = 750 K, h = 10.5 nm, and K_u/K_{bulk} = 0.5, there is no E_{th} more than 0.5, or no H_0 more than 0 that satisfies bER = 1E−3.

The results for various medium parameters, namely T_{cm}, h, and K_u/K_{bulk}, are summarized in Tables 2 and 3 for $m \times n$ = 3 × 3 = 9 grains/bit and $m \times n$ = 3 × 2 = 6 grains/bit, respectively. H_{zpeak} is the peak z component H_z of the initial readout field, and $H_0 \times H_{zpeak}$ is the minimum peak readout field that must be readable without error after 10 years of archiving. When adjacent track interference is considered, some grains are used as a guard band. Therefore, we also examined H_0, R_0, H_{zpeak}, and $H_0 \times H_{zpeak}$ for $m \times n$ = 2 × 3 = 6 grains in 9 grains/bit and $m \times n$ = 2 × 2 = 4 grains in 6 grains/bit.

The information during 10 years of archiving is stable for 9 grains/bit media with T_{cm} = 750 K, h = 10.5 nm, and K_u/K_{bulk} = 0.8 as shown in Table 2.

Table 2 Minimum normalized readout field H_0, information degradation rate R_0, initial readout field H_{zpeak}, and minimum readout field $H_0 \times H_{zpeak}$ after 10 years of archiving for 9 and 6 grains in 9 grains/bit.

9 grains / bit	D_m = 3.2 nm						
T_{cm} (K)	750	700	650	750	750	750	750
h (nm)	10.5	10.5	10.5	8.5	7.5	10.5	10.5
K_u / K_{bulk}	0.8	0.8	0.8	0.8	0.8	0.7	0.6
h / D_m	3.2	3.2	3.2	2.6	2.3	3.2	3.2
$K_{ueff}V / (kT)$ (T = 350 K)	113	96	79	91	80	99	84
9 grains							
$\quad H_0$	0.46	0.38	0.18	0.34	0.19	0.40	0.27
$\quad R_0$	0.71	5.8	64	12	47	4.0	26
$\quad H_{zpeak}$ (Oe)	1378	1278	1173	1320	1276	1378	1378
$\quad H_0 \times H_{zpeak}$ (Oe)	636	489	206	450	240	558	366
6 grains							
$\quad H_0$	0.34	0.23	n / a	0.18	n / a	0.26	0.08
$\quad R_0$	1.2	8.4	n / a	15	n / a	6.0	28
$\quad H_{zpeak}$ (Oe)	1190	1103	1012	1146	1112	1190	1190
$\quad H_0 \times H_{zpeak}$ (Oe)	405	254	n / a	201	n / a	308	96

Table 3 Minimum normalized readout field H_0, information degradation rate R_0, initial readout field H_{zpeak}, and minimum readout field $H_0 \times H_{zpeak}$ after 10 years of archiving for 6 and 4 grains in 6 grains/bit.

6 grains / bit	D_m = 4.2 nm					
T_{cm} (K)	600	750	750	650	650	750
h (nm)	10.5	6.5	10.5	7.5	10.5	7.5
K_u / K_{bulk}	0.8	0.8	0.5	0.8	0.6	0.6
h / D_m	2.5	1.6	2.5	1.8	2.5	1.8
$K_{ueff}V / (kT)$ (T = 350 K)	107	115	117	94	99	100
6 grains						
$\quad H_0$	0.31	0.35	0.36	0.21	0.27	0.27
$\quad R_0$	2.3	0.82	0.63	9.8	5.6	5.0
$\quad H_{zpeak}$ (Oe)	1057	1240	1371	1098	1167	1290
$\quad H_0 \times H_{zpeak}$ (Oe)	331	434	491	236	313	353
4 grains						
$\quad H_0$	0.14	0.21	0.22	0.02	0.08	0.09
$\quad R_0$	4.9	1.6	1.2	9.1	8.0	7.8
$\quad H_{zpeak}$ (Oe)	950	1127	1232	994	1049	1168
$\quad H_0 \times H_{zpeak}$ (Oe)	136	231	268	23	86	103

Although the T_{cm}, h, and K_u/K_{bulk} values can be reduced to 700 K, 8.5 nm, and 0.6, respectively, simultaneous reduction cannot be realized. The h/D_m value necessary for information stability is especially large due to the small grain size D_m of 3.2 nm. The medium parameters to be reduced must be selected depending on the difficulty of manufacturing the medium.

Since the mean grain size D_m for 6 grains/bit increases to 4.2 nm from 3.2 nm in 9 grains/bit as shown in Table 3, the degree of freedom in design increases. The grain area D_m^2 ratio is 1.68 and more than 9 / 6 = 1.5 between 6 and 9 grains/bit since the Δ_G value is independent of the grain number per bit.

3.2 Effective thermal stability factor

To enable us to interpret the above calculated results, we plot the H_0 and R_0 values against
$$K_{ueff}V/(kT) = (K_u - M_s H_d/2)(D_m \times D_m \times h)/(kT)$$
at 350 K in Figs. 3 and 4 for 9 and 6 grains/bit, respectively. All the calculated data for 9 and 6 grains in 9 grains/bit and for 6 and 4 grains in 6 grains/bit are on their lines. Furthermore, the H_0 and R_0 values for 6 grains in 9 and 6 grains/bit are the same as shown in Figs. 4 (a) and (b), respectively. H_0 and R_0 are functions of $K_{ueff}V/(kT)$ and grain number, and are independent of grain number per bit since $K_u \gg M_s H_d/2$ in K_{ueff}.
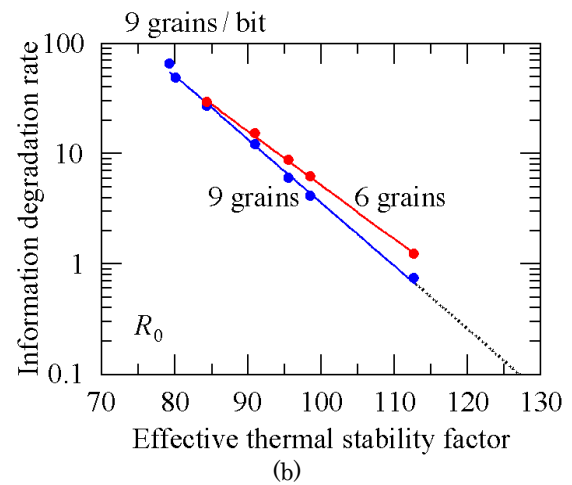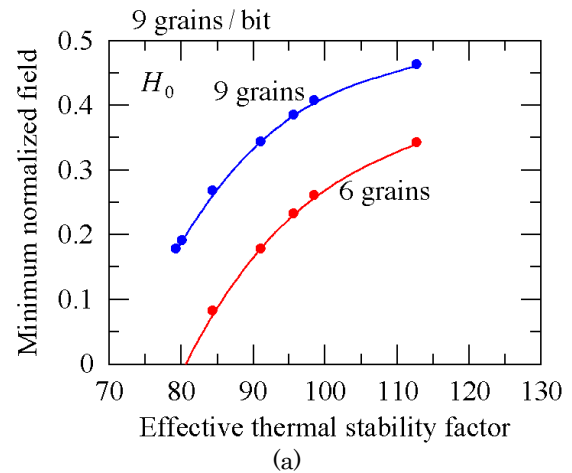

Fig. 3 (a) Minimum normalized readout field H_0 and (b) information degradation rate R_0 against effective thermal stability factor $K_{ueff}V/(kT)$ for 9 and 6 grains in 9 grains/bit.
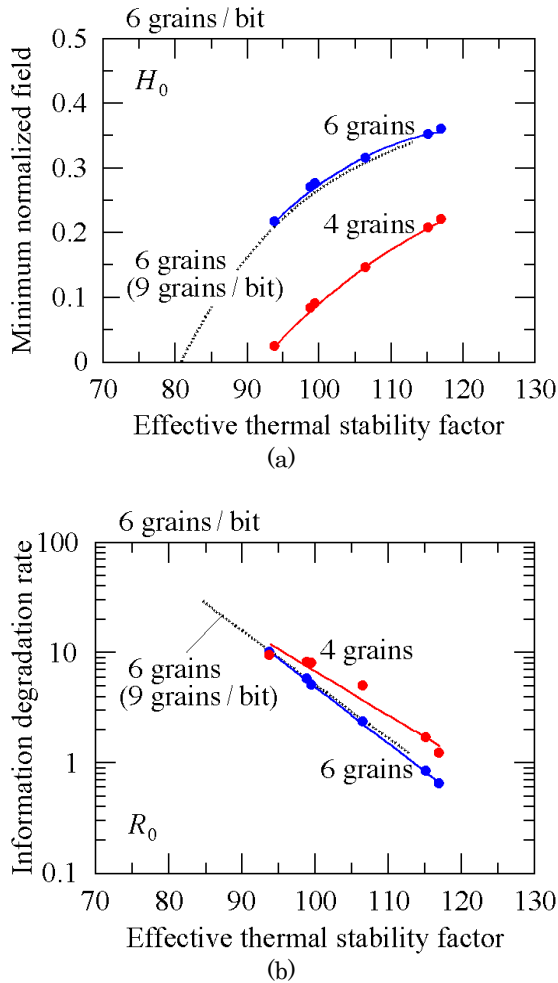
(a)

(b)

Fig. 4 (a) Minimum normalized readout field H_0 and (b) information degradation rate R_0 against effective thermal stability factor $K_{ueff}V/(kT)$ for 6 and 4 grains in 6 grains/bit.

The H_0 value for 9 grains is larger than that for 6 grains in 9 grains/bit as shown in Fig. 3 (a) due to a statistical factor. The statistical factor can be explained using the following example. If one bit contains many grains, the bER becomes low since the probability of a simultaneous error is very low for more than half of the grains in one bit. For example, when all the grains are assumed to be homogeneous, and P and E_{th} are 0.1 and 0.5, respectively, the bER calculated for 5 grains/bit is

$$\text{bER} = \sum_{k=3}^{5}\binom{5}{k}P^k(1-P)^{5-k} \approx 0.009. \qquad (12)$$

On the other hand, the bER for 9 grains/bit is

$$\text{bER} = \sum_{k=5}^{9}\binom{9}{k}P^k(1-P)^{9-k} \approx 0.0009, \qquad (13)$$

which is much lower than that for 5 grains/bit. Therefore, to obtain the same bER, P must be reduced for 5 grains/bit, and a larger $K_{ueff}V/(kT)$ value is necessary.

And the H_0 value for 6 grains in 9 grains/bit is larger than that for 4 grains in 6 grains/bit as shown in Fig. 4 (a). Although it is necessary to increase the $K_{ueff}V/(kT)$ value for 6 grains/bit to obtain the same H_0 value for 9

grains/bit, it is easy to increase the $K_{ueff}V/(kT)$ value for 6 grains/bit since the one grain area is 1.68 times larger. However, there is a concern that the readout SNR for 6 grains/bit is smaller than that for 9 grains/bit due to the small grain number.

A linear relationship was found between logarithmic R_0 and $K_{ueff}V/(kT)$, and the R_0 value decreases slightly in the order of 4, 6, and 9 grains as shown in Figs. 3 (b) and 4 (b). The $K_{ueff}V/(kT)$ value necessary for no information degradation is more than about 120.

The H_{zpeak} and $H_0 \times H_{zpeak}$ values are plotted against $K_{ueff}V/(kT)$ in Figs. 5 and 6 for 9 and 6 grains/bit, respectively. The lines in the figures are guides for the eye. The cause of data scattering is that H_0 is a function of $K_{ueff}V/(kT)$, and H_{zpeak} is a function of M_s, D_m, and h. And although the M_s value is a function of T_c, it is independent of K_u/K_{bulk}. Roughly, all calculation data for 9 and 6 grains in 9 grains/bit and for 6 and 4 grains in 6 grains/bit are on their lines as shown in Figs. 5 and 6, respectively.
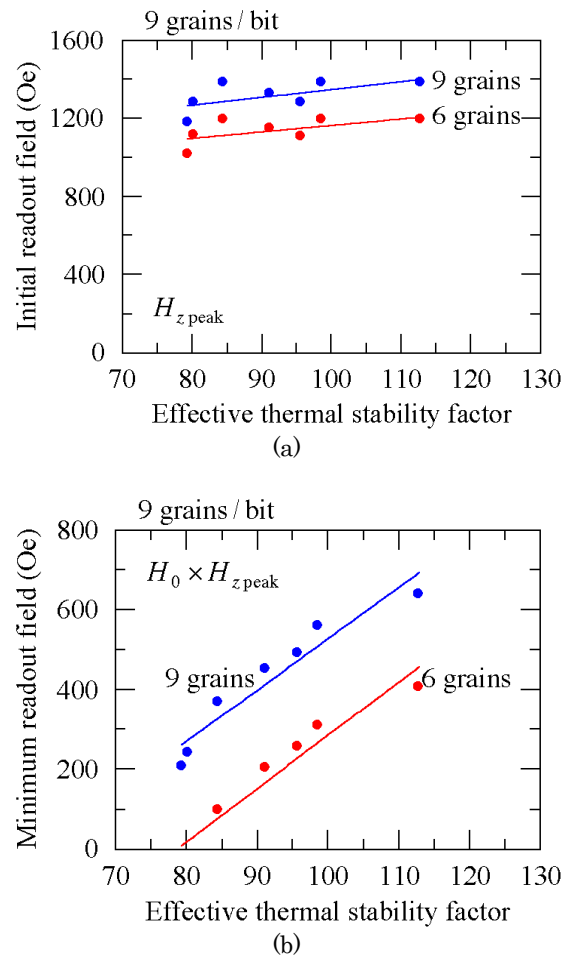

(a)

(b)

Fig. 5 (a) Initial readout field H_{zpeak} and (b) minimum readout field $H_0 \times H_{zpeak}$ against effective thermal stability factor $K_{ueff}V/(kT)$ for 9 and 6 grains in 9 grains/bit.
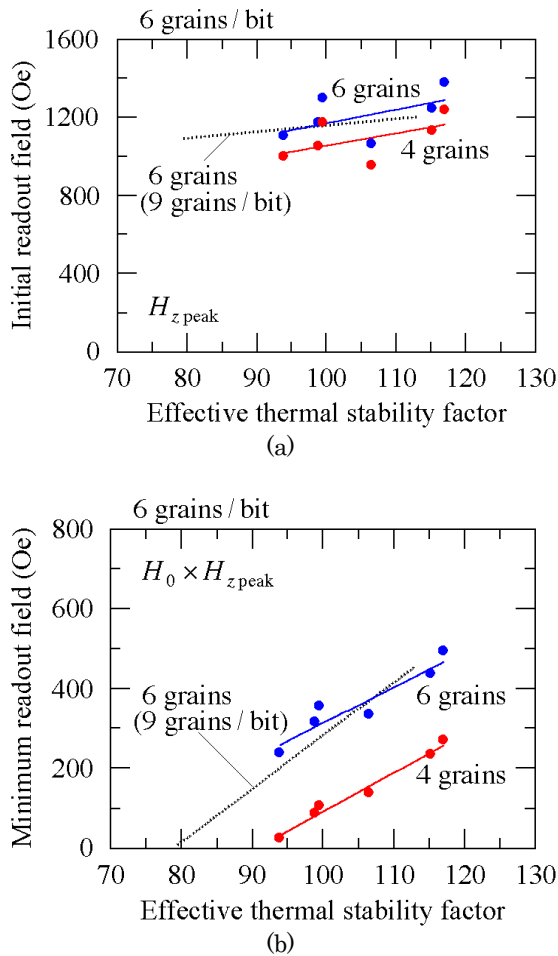
Fig. 6 (a) Initial readout field H_{zpeak} and (b) minimum readout field $H_0 \times H_{zpeak}$ against effective thermal stability factor $K_{ueff}V/(kT)$ for 6 and 4 grains in 6 grains/bit.

The $H_0 \times H_{zpeak}$ value for 9 grains is larger than that for 6 grains in 9 grains/bit as shown in Fig. 5 (b) since both H_0 and H_{zpeak} for 9 grains are larger than those for 6 grains as shown in Figs. 3 (a) and 5 (a). Furthermore, the $H_0 \times H_{zpeak}$ values for 6 grains in 9 and 6 grains/bit are roughly the same as shown in Fig. 6 (b).

There are many factors to be considered when designing the medium. A high T_{cm} is disadvantageous in terms of the heat resistance of the writing head and/or the surface lubricant. On the other hand, a low T_{cm} is disadvantageous in terms of information stability for 10 years of archiving since K_u at the storage temperature becomes small[3]. A low T_{cm} is also disadvantageous since the thermal gradient becomes small[7]. A larger h/D_m seems to make it too difficult to manufacture the medium. There is a concern that K_u decreases as D_m decreases.

We must comprehensively examine all the factors if we are to determine the medium parameters. Since these factors are currently being experimentally investigated by many researchers, it is currently impossible to determine the medium parameters. However, the above calculations will be useful for determining them in the future.

4. Conclusions

We examined the dependence of information stability for 10 years of archiving on various medium parameters, namely T_{cm}, h, and K_u/K_{bulk}, in 4 Tbpsi HAMR. As a result, we found that the minimum normalized readout field H_0 and information degradation rate R_0 are functions of the effective thermal stability factor $K_{ueff}V/(kT)$ and grain number, and are independent of grain number per bit since $K_u \gg M_s H_d/2$ in K_{ueff}. The $K_{ueff}V/(kT)$ value necessary for no information degradation is more than about 120. Furthermore, there is a weak correlation between the initial readout field H_{zpeak} or the minimum readout field $H_0 \times H_{zpeak}$ and $K_{ueff}V/(kT)$.

Although the T_{cm}, h, and K_u/K_{bulk} values can be reduced to 700 K, 8.5 nm, and 0.6, respectively, for 9 grains/bit, a simultaneous reduction cannot be realized. The h/D_m value necessary for information stability is especially large due to the small grain size D_m of 3.2 nm. Depending on the difficulty involved in manufacturing a medium, we must select the medium parameters to be reduced.

It is easy to increase the $K_{ueff}V/(kT)$ value for 6 grains/bit since the one grain area is 1.68 times larger.

References

1) S. H. Charap, P. -L. Lu, and Y. He: *IEEE Trans. Magn.*, **33**, 978 (1997).
2) T. Kobayashi, Y. Isowaki, and Y. Fujiwara: *J. Magn. Soc. Jpn.*, **39**, 8 (2015).
3) T. Kobayashi, Y. Nakatani, and Y. Fujiwara: *J. Magn. Soc. Jpn.*, **43**, 114 (2019).
4) M. Mansuripur and M. F. Ruane: *IEEE Trans. Magn.*, **MAG-22**, 33 (1986).
5) J. -U. Thiele, K. R. Coffey, M. F. Toney, J. A. Hedstrom, and A. J. Kellock: *J. Appl. Phys.*, **91**, 6595 (2002).
6) E. D. Boerner and H. N. Bertram: *IEEE Trans. Magn.*, **34**, 1678 (1998).
7) T. Kobayashi, Y. Nakatani, and Y. Fujiwara: *J. Magn. Soc. Jpn.*, **44**, 122 (2020).

<Paper>

A Consideration of Efficiency and Power Factor of IPM-type Magnetic-Geared Motor

K. Ito, K. Nakamura

Graduate School of Engineering, Tohoku University, *6-6-11 Aoba Aramaki Aoba-ku, Sendai, Miyagi 980-8579, Japan*

Magnetic-geared motors (MGMs) have attracted attention since their torque density is superior to conventional electric motors. Among the types of MGMs, an interior permanent magnet (IPM) type has a feature of high efficiency because the IPM-type can reduce the eddy current loss in magnets. On the other hand, in the IPM-type MGM, the PM motor part and the MG part magnetically interact with each other, which is called the magnetic interaction. In a previous paper, the influence of the magnetic interaction on the output torque was investigated. However, the influence on the power factor and the efficiency has not been clarified yet. This paper studies the influence of the magnetic interaction on the power factor and the efficiency of the IPM-type MGM. The influence of the magnetic interaction on the power factor is discussed by deriving a voltage equation of IPM-type MGM. Moreover, the power factor and the efficiency are calculated and measured to clarify a suitable current phase from the viewpoint of a high-power-factor and high-efficiency drive.

Key words: Magnetic-geared motor (MGM), Magnetic interaction, Efficiency, Power factor

1. Introduction

The electrification of vehicles and ships has been required to reduce the carbon dioxide emissions on the global environment. In many cases, a general drive system of electric vehicles and ships consists of an electric motor and a mechanical gearbox to obtain the desired speed and torque in terms of reducing size and weight. However, the mechanical gearbox has inherent problems due to mechanical contacts, e.g., acoustic noise, wear and tear, vibration, and periodical maintenance.

To solve the above problems, a magnetic-geared motor (MGM) has attracted attention [1]-[3]. An MGM consists of a permanent magnet (PM) motor and a flux-modulated type magnetic gear (MG). It can transmit the torque without any mechanical contacts by using an electromagnetic force. In addition, the MGM has the structure that a PM motor and an MG are magnetically integrated as a single electric machine so that it can offer a higher torque density than the conventional drive system. Hence, the MGM is expected to be put into practical use.

Fig. 1 shows a basic configuration of MGMs, which consist of a PM motor part and an MG part, and they share a single high-speed-rotor (HSR). The PM motor part consists of the armature and the shared HSR, while the MG part consists of the shared HSR, a magnetic modulator called pole-pieces (PP), and the low-speed-rotor (LSR). As shown in the figure, they can be classified roughly into two types in terms of the HSR structure. One is a surface permanent magnet (SPM) type, and the other is an interior permanent magnet (IPM) type [4]-[6].

Fig. 1 (a) shows the SPM-type MGM. It has permanent magnets on the surface of the HSR yoke. Thus, the PM motor part and the MG part are magnetically decoupled by the HSR yoke, so that magnetic fluxes from both parts do not influence each other. However, the SPM-type MGM causes a large eddy current loss in magnets of the HSR due to asynchronous harmonic fluxes [6].
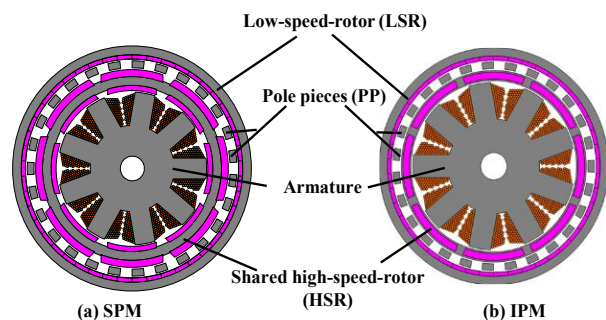
Corresponding author: K. Ito (e-mail: kouki.ito.t4@dc.tohoku.ac.jp).

Fig. 1 Basic configuration of magnetic-geared motors (MGMs).

Fig. 1 (b) shows the IPM-type MGM that permanent magnets are embedded in the HSR yoke. The efficiency of the IPM-type is higher than the SPM-type because the eddy current loss in magnets can be reduced by the embedding structure [6]. However, the PM motor part and the MG part magnetically interact with each other [7]. This interaction is called the magnetic interaction.

In previous studies, Refs. 7) and 8) have reported the magnetic interaction. However, these studies only discussed the relationship between the magnetic interaction and the output torque of the IPM-type MGM. It is concerned that the magnetic interaction influences not only the output torque but also the power factor and the efficiency. Thus, if the magnetic interaction is utilized effectively, the power factor and the efficiency of the IPM-type MGM will be further improved. However, the influence of the magnetic interaction on the power factor and the efficiency has not been clarified.

This paper investigates the influence of the magnetic interaction on the power factor and the efficiency of the IPM-type MGM. First, a voltage equation of the IPM-type MGM considering the magnetic interaction is derived to clarify the influence of the magnetic interaction on the power factor. Next, to verify the derived voltage equation, the power factor and the efficiency are calculated by a three-dimensional finite element method (3D-FEM). Finally, the experimental verification is carried out by using a prototype IPM-type MGM.

2. Derivation of Voltage Equation of IPM-type MGM Considering Magnetic Interaction

2.1 Conventional voltage equation

If the magnetic interaction does not occur, then the voltage equation of the MGM is the same as that of a conventional PM motor, which can be represented in the d-q axis coordinate system by

$$\begin{pmatrix} v_d \\ v_q \end{pmatrix} = \begin{pmatrix} R+pL_d & \omega_{eh}L_q \\ \omega_{eh}L_d & R+pL_q \end{pmatrix} \begin{pmatrix} i_d \\ i_q \end{pmatrix} + \omega_{eh} \begin{pmatrix} 0 \\ \psi_h \end{pmatrix}, \quad (1)$$

where the d- and q-axis components of currents and voltages are i_d, i_q, v_d, v_q, respectively. The phase resistance is R, and the amplitude of the flux linkage from the HSR magnet is ψ_h. The electric angular velocity of the HSR is ω_{eh}. The d- and q- axis inductances are L_d and L_q. A differential operator is $p (= d/dt)$. In general, the MGM is driven by the $i_d = 0$ control because the electrical property is similar to that of a conventional SPM-type PM motor [8].

In case of the PP are stationary, the gear ratio G_r is represented by using the pole-pairs of HSR p_h and LSR p_l, and the number of poles of PP n_{pp} as follows [9]:

$$G_r = \frac{p_h}{n_{pp}\text{-}p_h} = \frac{p_h}{p_l}. \quad (2)$$

When a three-phase ac current flows the armature windings, the rotating magnetic field is generated and the HSR is synchronously rotated. Then, the magnetic flux of the HSR is modulated by PP, and the LSR is rotated at a speed according to (2).

2.2 Derivation of voltage equation of IPM-type MGM

Fig. 2 denotes the schematic diagram of the IPM-type MGM. From the top, it shows LSR, PP, HSR, and the armature, respectively. Table 1 shows the parameters shown in Fig. 2. The solid line arrows indicate the magnetic flux of each rotor magnet. On the other hand, the dashed line arrows express the modulated magnetic flux by the PP. In the IPM-type MGM, as shown in the figure, the modulated magnetic flux of the LSR magnet ψ_{ml} reaches the armature due to the magnetic interaction. Hence, in addition to the armature fluxes $L_d i_d$, $L_q i_q$, and the magnetic flux of the HSR magnet ψ_h, the modulated magnetic flux of the LSR magnet ψ_{ml} also links with the armature winding. Accordingly, in order to derive the voltage equation of the IPM-type MGM, these four magnetic fluxes should be considered.

Fig. 3 indicates the vector diagram of the IPM-type MGM in the d-q axis coordinate system which rotates synchronously with the HSR. As described above, since the modulated magnetic flux of the LSR magnet reaches the armature, its magnetic flux is taken into consideration as the vector ψ_{ml} in the figure. The phase difference between ψ_{ml} and ψ_h is equal to the load angle δ.

As shown in the figure, the linkage flux of the armature winding ψ_o is determined by the sum of four magnetic fluxes $L_d i_d$, $L_q i_q$, ψ_h, and ψ_{ml}. Here, the phase of ψ_{ml} changes with the load angle δ, i.e. the load torque, and thereby the phase of ψ_o changes too. As a result, the

phase of the armature voltage v_a is varied since the phase difference between v_a and ψ_o is always 90 degrees. Consequently, it is found that the power factor angle Φ depends on the modulated magnetic flux ψ_{ml}.

Based on the above discussion, it can be concluded that the modulated magnetic flux ψ_{ml} influences the power factor due to the magnetic interaction. Moreover, the current phase angle β should be actively controlled so that the power factor is kept high, namely, the $i_d = 0$ control is not the most suitable way for the IPM-type MGM. It is understood from Fig. 3 that the d- and q-components of the modulated magnetic flux of the LSR magnet ψ_{mld} and ψ_{mlq} are given by

$$\begin{pmatrix} \psi_{mld} \\ \psi_{mlq} \end{pmatrix} = \begin{pmatrix} -\psi_{ml}\sin\delta \\ \psi_{ml}\cos\delta \end{pmatrix}. \quad (3)$$
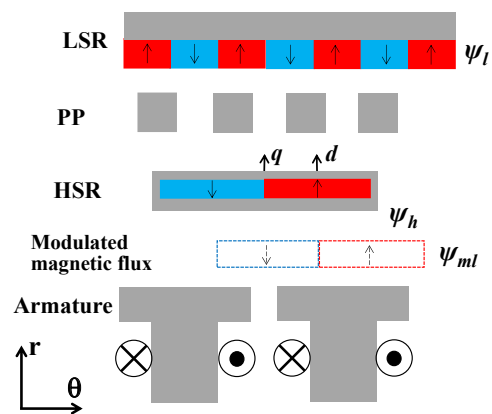

Fig. 2 Schematic diagram of the IPM-type MGM.

Table 1 Parameters shown in Figs 2 and 3.

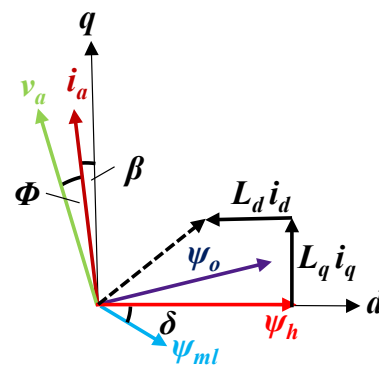|	
ψ_l	magnetic flux of the LSR magnet
ψ_h	magnetic flux of the HSR magnet
ψ_{ml}	modulated ψ_l
ψ_o	linkage flux of the armature winding $(L_d i_d + L_q i_q + \psi_h + \psi_{ml})$
v_a	armature voltage
i_a	armature current
β	current phase angle
Φ	power factor angle
δ	load angle of magnetic gear parts

Fig. 3 Vector diagram of the IPM-type MGM.

Finally, the voltage equation of the IPM-type MGM can be derived based on (1) and (3) as follows:

$$\begin{pmatrix} v_d \\ v_q \end{pmatrix} = \begin{pmatrix} R+pL_d & \omega_{eh}L_q \\ \omega_{eh}L_d & R+pL_q \end{pmatrix} \begin{pmatrix} i_d \\ i_q \end{pmatrix} + \omega_{eh} \begin{pmatrix} -\psi_{ml}\sin\delta \\ \psi_h + \psi_{ml}\cos\delta \end{pmatrix}. \qquad (4)$$

It is also understood from (4) that the armature voltages v_d, v_q depend on the modulated magnetic flux ψ_{ml}.

3. Investigation of Influence of Magnetic Interaction on Basic Characteristics of IPM-type MGM

3.1 Specifications of IPM-type MGM used for examinations

Table 2 shows the specifications of the IPM-type MGM shown in Fig. 1(b). The diameter is 140 mm, the axial length including the coil end is 36 mm, and the three air gap lengths are 1 mm each, respectively. The PM motor part is composed of the 9-slots armature with three-phase concentrated windings and the shared 4-pole-pairs HSR. The MG part is composed of the shared 4-pole-pairs HSR, the 23-pole-pairs LSR, and the 27-poles PP. Therefore, the gear ratio is 5.75 from (2). The material of each rotor magnets is sintered Nd-Fe-B. The material of the armature core, the HSR yoke, and the LSR yoke is 6.5%Si-Fe steel. The material of PP is a soft magnetic composite.

3.2 Influence on the phase of armature voltage

The phase of the armature voltage is calculated by 3D-FEM in various load angles, namely, in various load torques, to clarify the influence of the magnetic interaction on the armature voltage. The JMAG-Designer software ver. 19.0 is used for calculation by FEM. In 3D-FEM, the rotational speed and the current phase are kept constant (= 0 deg.).

Fig. 4 indicates the calculated fundamental component waveform of the armature voltage at various load angles of 0 (no-load), 30, 45, and 90 (full-load) degrees. An input current is also indicated in the figure as a reference of the phase. It is understood that the phase of the armature voltage is gradually shifted by increasing the load angles, i.e. the load torque. Thus, the validity of the discussion in Section 2.2 is proved.

3.3 Influence on the efficiency and the power factor

The power factor and the efficiency are calculated by 3D-FEM in various current phases and load angles. In the calculation of the efficiency, the copper loss, the iron loss, and the eddy current loss in magnets are considered, while the mechanical loss is neglected. Thus, the efficiency η is calculated by the following equation:

$$\eta = \frac{\omega_l T_l}{W_c + W_i + W_{em} + \omega_l T_l} \times 100 \ (\%), \qquad (5)$$

where the mechanical angular velocity of the LSR is ω_l, the torque of the LSR is T_l, the copper loss is W_c, the iron loss is W_i, and the eddy current loss in magnets is W_{em}, respectively. In 3D-FEM, the input current is an ideal

sinusoidal wave, namely, harmonic components are not considered due to the switching of the converter.

Fig. 5 indicates the calculated torque at various current phases and load angles. It is understood that the torque increases when the current phase is lagging, while decreases when it is leading. The reason is that the magnetic flux is strengthened in the lagging current phase while weakened in the leading current phase due

Table 2 Specifications of the IPM-type MGM used for examinations.

Outer diameter of LSR	140 mm
Axial length	36 mm
Outer diameter of stator	101 mm
Number of turns/pole	59 turns/pole
Winding diameter	1.2 mm
Winding space factor	46.1%
HSR magnet pole pairs	4
LSR magnet pole pairs	23
PP number of poles	27
Radial length of HSR magnets	4 mm
Radial length of LSR magnets	4 mm
Radial length of PP	2.5 mm
Gear ratio	5.75
Gap length	1.0 mm × 3
Material of magnet	Sintered Nd-Fe-B
Material of iron core	6.5%Si-Fe steel
Material of PP	Soft magnetic composite
HSR rotational speed	3000 rpm
LSR rotational speed	-521.7 rpm

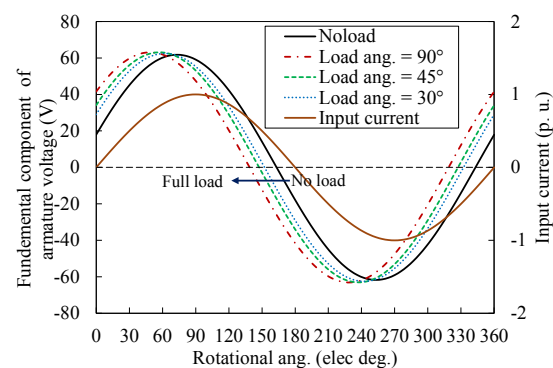**Fig. 4** Calculated waveforms of the armature voltage at various load angles.
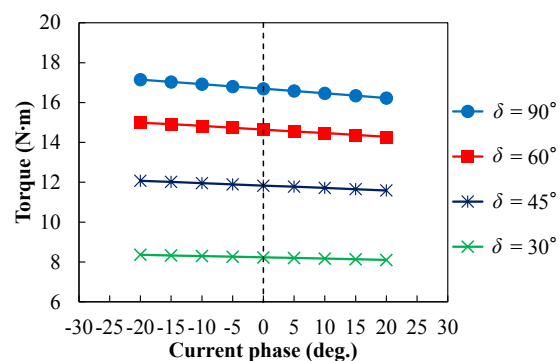

Fig. 5 Calculated torque at various current phases and load angles.

to the magnetic interaction[7]. As shown in the figure, the maximum torque calculated by 3D-FEM is about 17 N·m.

Fig. 6 shows the calculated copper loss at various current phases and load angles. The figure reveals that the copper loss becomes minimum at the current phase of around zero since the PM motor part of the IPM-type MGM has almost the same structure as the conventional SPM-type PM motor. In addition, the copper loss at the leading current phase is smaller than the one at the lagging current phase due to reluctance torque. As shown in Fig. 1(b), the iron yoke of HSR is thin and saturated by HSR magnets. Therefore, HSR has a magnetic saliency, by which the leading current can generate larger reluctance torque than the lagging current, which results in reducing the input current when it is leading.

Fig. 7 indicates the iron loss at various current phases and load angles. It is understood that iron loss increases when the current phase decreases, while decreases when the current phase increases. The reason is that the magnetic flux is strengthened in the lagging current phase while weakened in the leading current phase in the same way as the torque shown in Fig. 5. In addition, the iron loss is decreased by increasing the load angle when the current phase is constant. This is because the phase difference of fluxes between HSR and LSR magnets increases when the load angle increases, which results in decreasing the combined flux.

Fig. 8 shows the eddy current loss in magnets at various current phases and load angles. It can be found

that the eddy current loss in magnets increases when the current phase decreases, while decreases when the current phase increases in the same way described in the torque and the iron loss shown in Figs. 5 and 7. It can be considered that the armature flux influences the asynchronous harmonic flux which causes the eddy current loss in magnets. Accordingly, the asynchronous harmonic flux is increased at a lagging current phase, while decreased at a leading current phase. Furthermore, it is understood that the eddy current loss in magnets changes with the load angle when the current phase is constant. The reason is that the armature flux affects the asynchronous harmonic flux as described above, so that the eddy current loss in magnets is larger at a heavy load of a large load angle.

Fig. 8 Calculated eddy current loss in magnets at various current phases and load angles.

Fig. 9 Calculated efficiency at various current phases and load angles.

Fig. 6 Calculated copper loss at various current phases and load angles.
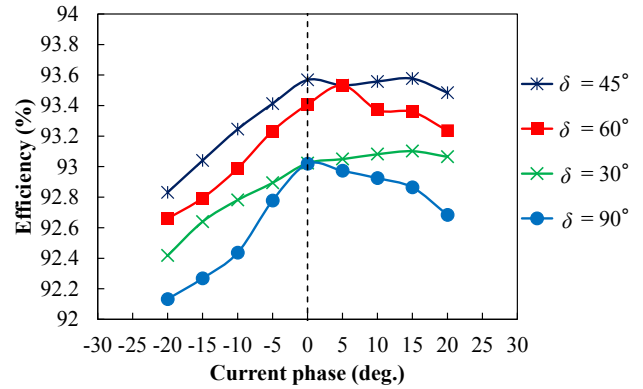
Fig. 7 Calculated iron loss at various current phases and load angles.
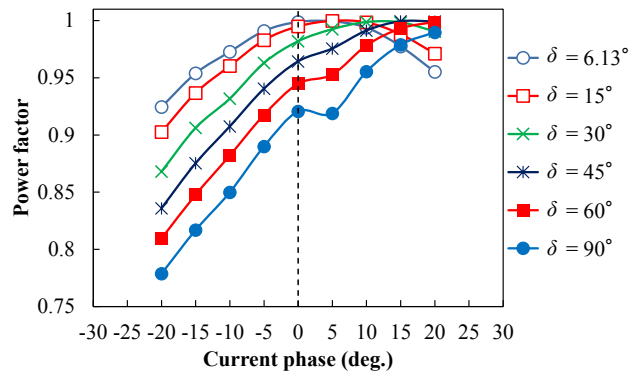

Fig. 10 Calculated displacement power factor at various current phases and load angles.

Fig. 9 indicates the calculated efficiency at various current phases and load angles obtained from Eq. (5). The figure reveals that the efficiency is high when the current phase is zero, and that it is also the same or higher when the current phase is leading. On the contrary, the efficiency is low in the lagging current phase. That is because the torque and the iron and eddy current losses increase when the current is lagging as shown in Figs. 5, 7, and 8, however, the increasing rate of losses is higher than that of torque. Moreover, it can be seen that the highest point of efficiency gets close to a current phase of zero as the load angle increases. The reason is that the copper loss remarkably increases when the load angle increases as shown in Fig. 6. Thus, the copper loss becomes major, and the efficiency is maximized around a current phase of zero. From the above discussion, it is revealed that the zero or leading current phase is more suitable for the high efficiency drive of the IPM-type MGM.

Fig. 10 shows the displacement power factor at various current phases and load angles. The figure reveals that the power factor becomes maximum at the current phase of around zero when the load angle, i.e. the load torque is small, while when the load angle is increasing, the maximum point of the power factor is gradually shifted to the leading current phase region. Hence, in the IPM-type MGM, it can be concluded that the leading current phase control is better than the $i_d = 0$ control from the viewpoint of the power factor and the efficiency.

4. Experimental Verification

In this chapter, to prove the validity of the calculation results, the power factor and the efficiency are measured by using the prototype IPM-type MGM.

Fig. 11 indicates the configuration of the experimental setup. It consists of the prototype IPM-type MGM, the torque detector, the hysteresis brake, the dc supply, the three-phase converter, and the power meter, respectively. The prototype IPM-type MGM is controlled by the vector control, and the position of the HSR is detected by a hall sensor. In the experiment, the rotational speed of the HSR is controlled to be 3000 rpm, and the load torque is set to be 2, 4, 6, 8, and 10 N·m.

Fig. 12 shows the measured efficiency at various current phases and load torques. The measured results, which have over 85% efficiency, are plotted. The figure reveals that the measured efficiency is lower than the calculated one because the mechanical loss, the eddy current loss in the housing, and the harmonic iron loss caused by PWM switching are ignored in 3D-FEM. In addition, it is understood that the measured efficiency at the leading current phase is higher, which is slightly different from the calculated one shown in Fig. 9. This is because the calculated copper loss is obviously larger than the calculated iron loss in 3D-FEM. On the other hand, the difference between the measured copper and iron losses is small since the eddy current loss in the

housing, and the harmonic iron loss caused by PWM switching are included in the experiment. Accordingly, the measured efficiency is the highest at the leading current phase. However, it can be seen that the overall trend of the measured efficiency is in good agreement with the calculated one.

Fig. 13 indicates the displacement power factor at various current phases and load torques. It is understood from the figure that the power factor decreases when the load torque, i.e., the load angle increases, and that the power factor reaches almost 1.0 when the current phase is leading. The figure reveals
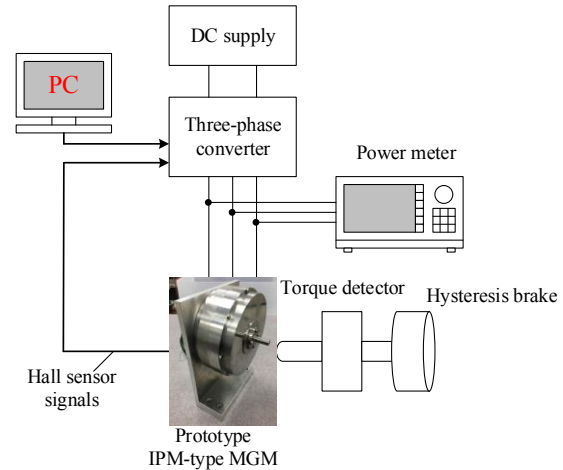

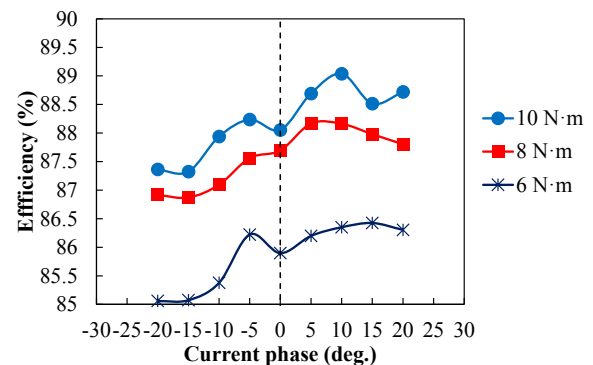**Fig. 11** Configuration of the experimental setup.

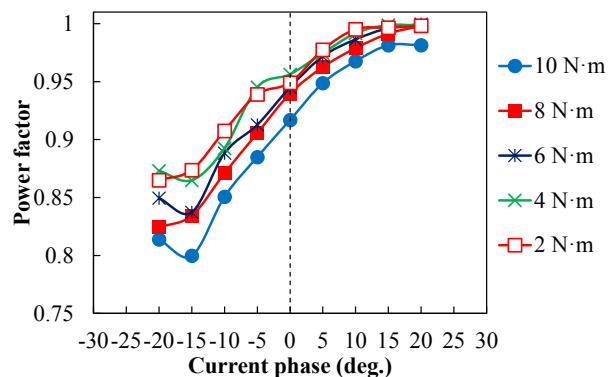**Fig. 12** Measured efficiency at various current phases and load torques.

Fig. 13 Measured displacement power factor at various current phases and load torques.

that the trend of the measured power factor is in good agreement with the calculated one shown in Fig. 10.

Hence, it is proved in the experiment that the leading current phase control is more suitable than the $i_d = 0$ control from the viewpoint of the power factor and the efficiency.

5. Conclusion

This paper presented the influence of the magnetic interaction on the power factor and the efficiency of the IPM-type MGM.

Based on the conventional voltage equation, the voltage equation of the IPM-type MGM was derived considering the modulated magnetic flux of the LSR magnet. In addition, the vector diagram of the IPM-type MGM was described based on the proposed equation. As a result, it was clear that the power factor changes with the load angle due to the magnetic interaction.

Next, the power factor was calculated by 3D-FEM to prove the validity of the proposed equation. Moreover, the efficiency was calculated to clarify the suitable current phase for a high-efficiency drive. As a result, the validity of the proposed equation was proved, and it was clarified that the leading current phase control is better than the conventional $i_d = 0$ control from the viewpoint of the power factor and the efficiency.

Finally, the validity of the calculated results was proved by the experiment of the prototype IPM-type MGM.

References

1) K. T. Chau, Z. Dong, J. Z. Jiang, L. Chunhua, and Z. Yuejin: *IEEE Trans. Magn.*, **43**, 2504-2506 (2007).
2) K. Atallah, J. Rens, S. Mezani, and D. Howe: *IEEE Trans. Magn.*, **44**, 4349-4352 (2008).
3) K. Ito, T. Kadomatsu, K. Obana, and K. Nakamura: *International Journal of Applied Electromagnetics and Mechanics*, **64**, 157-163 (2020).
4) T. V. Frandsen, L. Mathe, N. I. Berg, R. K. Holm, T. N. Matzen, P. O. Rasmussen, and K. K. Jensen: *IEEE Trans. Ind. Appl.*, **51**, 1516-1525 (2015).
5) S. Gerber and R.-J. Wang: *IEEE Trans. Magn.*, **51**, Art. no. 8107010 (2015).
6) K. Ito, T. Kadomatsu, and K. Nakamura: *J. Magn. Soc. Jpn.* (*Special Issues*), **3**, 69-73 (2019) (in Japanese).
7) K. Ito and K. Nakamura: *IEEE Trans. Magn.*, **57**, Art. no. 8202005 (2020).
8) E. Morimoto, N. Niguchi, and K. Hirata: *J. JSAEM*, **26**, 15-21 (2018) (in Japanese).
9) K. Atallah and D. Howe: *IEEE Trans. Magn.*, **37**, 2844-2846 (2001).